Titre: Title:	Effect of Surface Roughness on Aircraft Stall
Auteur: Author:	Charles Bilodeau-Bérubé
Date:	2023
Type:	Mémoire ou thèse / Dissertation or Thesis
Référence: Citation:	Bilodeau-Bérubé, C. (2023). Effect of Surface Roughness on Aircraft Stall [Mémoire de maîtrise, Polytechnique Montréal]. PolyPublie. https://publications.polymtl.ca/10827/

URL de PolyPublie: PolyPublie URL:	https://publications.polymtl.ca/10827/
Directeurs de recherche: Advisors:	Éric Laurendeau
Programme: Program:	Génie aérospatial

POLYTECHNIQUE MONTRÉAL
affiliée à l'Université de Montréal

Effect of Surface Roughness on Aircraft Stall

CHARLES BILODEAU-BÉRUBÉ
Département de génie mécanique

Mémoire présenté en vue de l'obtention du diplôme de *Maîtrise ès sciences appliquées*
Génie aérospatial

Janvier 2023

POLYTECHNIQUE MONTRÉAL
affiliée à l'Université de Montréal

Ce mémoire intitulé :

Effect of Surface Roughness on Aircraft Stall

présenté par **Charles BILODEAU-BÉRUBÉ**
en vue de l'obtention du diplôme de *Maîtrise ès sciences appliquées*
a été dûment accepté par le jury d'examen constitué de :

Roberto PAOLI, président
Éric LAURENDEAU, membre et directeur de recherche
Yannick HOARAU, membre

DEDICATION

To Professor Éric Laurendeau,

I am writing these few words to thank you
For your passion for aerodynamics,
For your unwavering support,
For your inspiring metaphors,
For your wisdom and kindness.

You have helped me grow as a scientist,
And I am grateful for everything I have learned from you.
You have sparked in me a love for science
And for life itself.

You are an exceptional mentor and role model,
And I am fortunate to have had the opportunity to know you.
With great gratitude,
I dedicate my thesis to you.

With warmest thanks,

Charles

DÉDICACE

Au professeur Éric Laurendeau,

Je vous écris ces quelques mots pour vous remercier
Pour votre passion pour l'aérodynamique
Pour votre soutien indéfectible
Pour vos métaphores inspirantes
Pour votre sagesse et votre bienveillance

Vous m'avez fait grandir en tant que scientifique
Et je suis reconnaissant pour tout ce que j'ai appris grâce à vous
Vous avez suscité en moi un amour pour la science
Et pour la vie elle-même

Vous êtes un mentor et un modèle exceptionnel
Et je suis chanceux d'avoir eu l'opportunité de vous connaître
Et c'est avec une grande gratitude
Que je dédie mon mémoire à vous

Avec mes remerciements les plus chaleureux,

Charles

ACKNOWLEDGEMENTS

The research work described in this thesis is funded by NSERC/CRIAQ/Bombardier Industrial Research Chair. The author would like to thank Dr. Rolf Radespiel (TU BS), Martin Kruse (DLR) and Cornelia Grabe (DLR) for providing the geometry and documentation for their sickle wing

RÉSUMÉ

Les simulations numériques sont largement utilisées dans l'analyse et la conception d'avions pour prédire des phénomènes complexes et réduire la nécessité de tests physiques. Cependant, certains comportements physiques demeurent difficiles à prédire avec suffisamment de précision, tels que la rugosité qui se développe sur la surface des ailes d'avions lorsque des contaminants comme la glace, la saleté ou les insectes morts s'y accumulent. Cette augmentation de la rugosité peut avoir un impact négatif sur les performances aérodynamiques, affectant la certification de l'avion et la sécurité des passagers.

L'objectif principal de cette recherche est de modéliser la rugosité de surface dans un logiciel RANS maison appelé CHAMPS afin de valider ses effets sur la turbulence, la traînée et les caractéristiques de décrochage. Pour ce faire, il est nécessaire de modéliser en premier les effets de la turbulence et de la transition pour servir comme base à l'implémentation du modèle de rugosité.

La première partie présente une revue de la littérature, discutant des méthodes alternatives, en se concentrant sur les modèles Reynold-Average Navier-Stokes. La seconde partie présente la méthodologie, expliquant les stratégies utilisées pour l'implémentation des modèles de turbulence, de transition et de rugosité. Pour simuler la turbulence, les équations des modèles de turbulence $k-\omega$ SST et Spalart-Allmaras sont intégrées dans CHAMPS en utilisant la méthode des volumes finis. Ensuite, les effets de transition sont ajoutés en utilisant une approche de modèle de transition basée sur des corrélations locales (LCTM) en implémentant le modèle γ-$\tilde{R}e_{\theta t}$ qui est ensuite couplé à chacun des modèles de turbulence. Ils sont désignés comme les modèles $k\omega$-γ-$\tilde{R}e_{\theta t}$ et SA-γ-$\tilde{R}e_{\theta t}$. Des variantes des corrélations F_{length} et Re_{θ_c} sont implémentées pour éliminer les discontinuités créées par les fonctions min et max. De plus, une investigation est menée pour tester le potentiel d'étalonnage de certaines constantes de la corrélation F_{onset}, montrant que l'augmentation de la valeur de deux constantes peut décaler la transition vers l'aval. Pour le modèle SA-γ-$\tilde{R}e_{\theta t}$, l'intensité de la turbulence est supposée constante, et la correction de séparation induite est désactivée, car elle n'est nécessaire que pour le modèle $k\omega$-γ-$\tilde{R}e_{\theta t}$.

Une extension est ajoutée aux modèles pour inclure la transition induite par un écoulement transversal, observé sur les géométries 3D. Enfin, les effets de rugosité sont implémentés en utilisant un modèle d'amplification de la rugosité, ce qui nécessite la modification de la condition limite de surface afin d'inclure la rugosité et nécessite l'ajout d'une équation de transport supplémentaire pour influencer la transition. Des conditions limites de surface rugueuses différentes sont utilisées pour les deux modèles, et une modification a été implémentée pour

inclure une rugosité au bord d'attaque.

La troisième partie se concentre sur les résultats de la transition. Tout d'abord, les modèles $k\omega$-γ-$\tilde{R}e_{\theta t}$ et SA-γ-$\tilde{R}e_{\theta t}$ sont comparés et validés sur des cas de plaques plates et de profils d'aile en comparant les prédictions de l'emplacement de la transition avec les données expérimentales de la littérature. La prédiction de l'emplacement de la transition à différents angles d'attaque est validée pour trois mécanismes de transition : transition naturelle, transition induite par séparation et transition de contournement. Bien que les emplacements de transition soient bien prédits pour les deux modèles en général, la transition naturelle présente moins de précision et est plus sensible à la résolution du maillage.

Une enquête est menée pour déterminer la cause de la transition naturelle précoce observée avec le modèle SA-γ-$\tilde{R}e_{\theta t}$ et montre que le mauvais calibrage de l'effet du rapport de viscosité est ce qui cause le décalage. La solution proposée consiste à calibrer une constante de l'équation F_{onset} qui a amélioré les résultats pour la transition naturelle.

Pour valider les résultats de la transition induite par l'écoulement transversal, deux cas 3D sont utilisés : la "prolate spheroid" et le "sickle wing". Pour la spheroid, la prédiction de la transition corresponds aux données expérimentales, surtout pour le modèle $k\omega$-γ-$\tilde{R}e_{\theta t}$. Pour le "sickle wing", deux topologies de maillage différentes sont utilisées dans la comparaison des modèles. Le modèle $k\omega$-γ-$\tilde{R}e_{\theta t}$ se comporte mieux pour prédire la forme particulière de la ligne de transition, par contre le modèle est très sensible à la topologie de maillage.

La quatrième partie présente les résultats de l'effet de la rugosité de surface sur la turbulence, la traînée et les caractéristiques de décrochage. Le décrochage est sur-prédit pour toutes les simulations, comme on s'y attend avec les modèles RANS. Néanmoins, l'effet de la rugosité sur la réduction de la portance et l'augmentation de la traînée sont bien représentés, en particulier pour le modèle SA-γ-$\tilde{R}e_{\theta t}$.

Enfin, la cinquième partie présente les conclusions et les travaux futurs. Dans l'ensemble, cette recherche présente une implémentation réussie des modèles de turbulence, de transition et de rugosité. Le modèle SA-γ-$\tilde{R}e_{\theta t}$ est recommandé par rapport au modèle $k\omega$-γ-$\tilde{R}e_{\theta t}$ pour sa meilleure performance numérique, son calibrage plus facile et sa meilleure précision pour l'effet de la rugosité. La principale limite de ce projet est l'incertitude quant à la précision des corrélations empiriques utilisées dans les modèles de transition, qui ne capturent pas la physique complète de la transition et qui sont basées sur des données expérimentales limitées. Dans les travaux futurs, ces modèles devront être validés davantage sur des cas plus complexes et étendus pour étudier d'autres aspects de la performance de l'aéronef affectés par la rugosité de la surface, en utilisant des approches de modélisation plus complètes pour capturer la physique totale de la transition.

ABSTRACT

Numerical simulations are widely used in the analysis and design of aircraft to predict complex phenomena and reduce the need for physical testing. However, some physical behaviors remain difficult to predict with sufficient accuracy, such as the roughness that develops on the surface of aircraft wings when contaminants like ice, dirt of dead bugs accumulate. This increase roughness can have negative impact on the aerodynamic performance, affecting the certification of the aircraft and the safety of all passengers.

The main objective of this research is to model the surface roughness in an in-house RANS software named CHAMPS in order to validate its effects on the turbulence, drag and stall characteristics. To do so, the turbulence and transition from laminar to turbulent flow effects must be modelled to serve as a foundation for the roughness implementation.

The first part presents a literature review, discussing alternative methods, focusing on the Reynold-Average Navier-Stokes models. The second part presents the methodology, explaining the strategies used for the implementation of the turbulence, transition and roughness models. To simulate the turbulence, the $k-\omega$ SST and Spalart-Allmaras turbulence models equations are incorporated into CHAMPS using the Finite Volume Method. Next, the transition effects are added using a Local Correlation-Based Transition Model (LCTM) approach by implementing the γ-$\tilde{Re}_{\theta t}$ model which is coupled with each turbulence model. They are referred to as the $k\omega$-γ-$\tilde{Re}_{\theta t}$ and SA-γ-$\tilde{Re}_{\theta t}$ models. Smooth variants of the F_{length} and Re_{θ_c} correlations are implemented to eliminate discontinuities created by min and max functions. Additionally, an investigation is conducted to test the calibration potential of some constants of the F_{onset} correlation, showing that increasing the value of two of the constants can push the transition downstream. For the SA-γ-$\tilde{Re}_{\theta t}$ model, a constant turbulent intensity is assumed, and the separation-induced correction is disabled since it is only needed with the $k\omega$-γ-$\tilde{Re}_{\theta t}$ model.

A crossflow extension is added to the models to account for crossflow-induced transition seen on 3D bodies. Finally, the roughness effects are implemented using a roughness amplification model, which required the modification of the wall boundary condition to include roughness and adds an extra transport equation to influence the transition. Different rough wall boundary conditions are used for both models, and a modification was implemented to account for leading edge roughness.

The third part focuses on the transition results. First, the $k\omega$-γ-$\tilde{Re}_{\theta t}$ and SA-γ-$\tilde{Re}_{\theta t}$ models are compared and validated on flat plate and airfoil cases by comparing the transition location

predictions with experimental data from the literature. The transition location prediction at different angles of attack is validated for three transition mechanisms: natural transition, separation-induced transition, and bypass transition. While the transition locations are well predicted for both models in general, the natural transition exhibits less accuracy and is more sensitive to mesh resolution.

An investigation is conducted to determine the cause of the early natural transition seen with the SA-γ-$\tilde{R}e_{\theta t}$ model and shows that the improper calibration of the effect of the viscosity ratio is what causes the offset. The proposed solution is to calibrate a constant of the F_{onset} equation which improved the results of natural transition.

For the results of the crossflow-induced transition, two 3D cases are used for validation: the inclined prolate spheroid and the sickle wing. For the spheroid, the prediction of the transition matches well with the experimental data, particularly for the $k\omega$-γ-$\tilde{R}e_{\theta t}$ model. For the sickle wing, two different mesh topologies are used in the comparison of the models. The $k\omega$-γ-$\tilde{R}e_{\theta t}$ model performs better at predicting the particular shape of the crossflow-induced transition line, but is very sensitive to the mesh topology.

The fourth part presents the results of the roughness implementation and its effects on turbulence, drag, and stall characteristics. The stall is over-predicted for all simulations, as it is expected with RANS models. Nevertheless, the effect of roughness on reducing lift and increasing drag is well represented, particularly for the SA-γ-$\tilde{R}e_{\theta t}$ model.

Finally, the fifth part presents the conclusions and future work. Overall, this research presents a successful implementation of turbulence, transition, and roughness models. The SA-γ-$\tilde{R}e_{\theta t}$ model is recommended over the $k\omega$-γ-$\tilde{R}e_{\theta t}$ model for its higher numerical performance, easier calibration, and better accuracy for the effect of roughness. The main limitation of this thesis is the uncertainty in the accuracy of the empirical correlations used in the transition models, which do not capture the complete physics of the transition and are based on limited experimental data. In future work, these models can be further validated in more complex cases and extended to investigate other aspects of aircraft performance affected by surface roughness, using more comprehensive modelling approaches to capture the full physics of the transition.

TABLE OF CONTENTS

LIST OF TABLES

LIST OF FIGURES

LIST OF SYMBOLS AND ACRONYMS

RANS	Reynolds-averaged Navier–Stokes
CFD	Computional Fluid Dynamics
ρ	density $[kg/m^3]$
α	angle of attack (AoA) $[^\circ]$
u_i	mean velocity component $[m/s]$
U	mean velocity vector
U_∞	free-stream mean velocity $[m/s]$
d	wall distance $[m]$
$\mathrm{d}t$	time step $[s]$
x, y, z	cartesian coordinate $[m]$
k	turbulent kinetic energy $[m^2/s^2]$
ω	dissipation rate $[1/s]$
A_r	roughness amplification factor
γ	intermittency $[-]$
M	Mach number $[-]$
Re	Reynold number $[-]$
$\tilde{R}e_{\theta t}$	transported quantity of the local transition onset momentum-thickness Reynolds number $[-]$
$Re_{\theta t}$	transition onset momentum-thickness Reynold number $[-]$
Tu	turbulence intensity $[\%]$
β	$\frac{\mu_t}{\mu}$ $[-]$
Ω	vorticity magnitude $[m/s]$
S	strain magnitude $[m/s]$
μ	molecular viscosity $[kg/m/s]$
μ_t	eddy viscosity $[kg/m/s]$
$\tilde{\nu}$	Spalart-Allmaras turbulence field variable
c_{opt}	optimized constants $[-]$
x_{tr}	transition onset location $[m]$
C_f	friction coefficient $[-]$
C_D	drag coefficient $[-]$
C_{Dp}	pressure drag coefficient $[-]$
C_L	lift coefficient $[-]$
RT	viscosity ratio $[-]$

LIST OF APPENDICES

CHAPTER 1 INTRODUCTION

1.1 Context

Turbulent flow is a common phenomenon observed around many solid body in motion relatively to a fluid. It can be observed in the air around helicopters and aircraft, but also in the water around boats, for example. In the context of an aircraft, contaminants such as ice, dirt or dead insects increase the surface roughness which affect the skin friction and the growth of the turbulent boundary layer. It changes the performance of the aircraft during cruise flight, but also during take-off or landing when the angle of attack of the aircraft is high. This thesis focuses on the modelling of the turbulent flow and effect of surface roughness, and how effective the models can predict the stall phenomena.

1.2 Basic Concepts

This section explains some concepts related to understanding turbulent flow and how it influences the aerodynamic performance of an aircraft.

1.2.1 Stall

The stall in the context of an aircraft is when increasing the angle of attack relative to the wind reaches a critical angle where the lift starts decreasing instead of increasing. This dangerous phenomenon is caused by the flow separation around the wing. The prediction of the stall characteristics are important to design aircraft capable of reaching higher lift, especially during the take-off and landing phases.

1.2.2 Laminar and Turbulent Flows

Laminar flow is characterized by a steady, smooth and regular motion of the fluid along the streamline [7]. On the contrary, turbulent flow is unsteady, random and moves in a chaotic motion [8]. When approaching a wall, the turbulent flow has a velocity that slowly decreases and then rapidly decreases to zero near the surface. In contrast, the velocity of the laminar flow decreases more gradually. This affects the wall shear stress, τ_ω, which is consequently higher for the turbulent flow. Therefore, having laminar or turbulent flow has a major impact on aerodynamic performance [7]. Turbulent flow has higher friction drag

and increased heat transfer rate, but laminar boundary layer will be more sensitive to the boundary layer separation, provoking stall at lower angles of attacks.

1.2.3 Natural Transition

Transition from laminar to turbulent flow can be triggered by different mechanisms. One common type of transition is called natural transition which is caused by a phenomenon named Tollmien-Schlichting waves [Schlichting, 1979]. These waves are unstable disturbances caused by the viscosity of the flow in the laminar boundary layer. They start to grow slowly into turbulent spots until the flow becomes fully turbulent [9].

1.2.4 Separation-Induced Transition

Separation-induced transition is another type of mechanism and it occurs when the laminar boundary layer separates forcing the transition to turbulent flow. Sometime the boundary layer will reattach forming a separation bubble causing the flow direction to be reversed near the surface wall.

1.2.5 Bypass Transition

This type of transition occurs when the flows directly transition from laminar to turbulent by skipping the natural pre-transitional events such as the growth of the Tollmien-Schlichting waves [9]. The freestream turbulence intensity needs to be higher than 1% except when the bypass transition is caused by surface roughness [9].

1.2.6 Crossflow-Induced Transition

Another type of disturbance that can cause transition similar to Tollmien-Schlichting waves are the instabilities caused by the crossflow on 3D bodies. The growth of turbulence is excited by the velocity component in the crossflow direction [9], causing the transition to occur before the other transition mechanisms. Note that the surface roughness can also amplify the crossflow instabilities.

1.2.7 Surface roughness

The surface roughness of a solid body can be increased by the presence of contaminants on its surface. This increase in roughness can lead to an increase in shear stress, which can amplify various transition mechanisms. In particular, the growth of Tollmien-Schlichting waves can

be accelerated, leading to an earlier natural transition. The increase in shear stress can also cause the boundary layer separation of the flow to occur earlier, reducing lift and increasing drag. This can affect the stall characteristics and control of an aircraft. Additionally, surface roughness can cause bypass transition and increase crossflow instabilities.

1.3 Problem Statement

Numerical simulations are used by aircraft manufacturers to predict the performances of aircraft throughout the design process. This strategy decreases the cost of the development by reducing the needs to do physical tests to measure the performance of the product [10]. For an aircraft, these tests can be wind tunnel experiments or flight tests and are very expensive compared to numerical simulations. One of the problems is that the aircraft manufacturers are unable to completely rely only on numerical simulations since they cannot predict yet certain phenomena accurately enough.

One phenomenon that is still challenging to predict using computational fluid dynamics (CFD) methods is the effect on the aerodynamic performance of the accumulation of ice and other contaminants like dead insects or dirt on the surface of the aircraft, especially on the leading edge of the wings [11]. The aircraft manufacturers want to design laminar wings that produce less turbulent flow for the ongoing effort in reduction in emissions and fuel burn of new aircraft while ensuring the safety and performance of the aircraft . However, these contaminants increase the surface roughness which impacts the transition location from laminar to turbulent flow, which has a strong influence on the drag of the body [11]. Moreover, the surface roughness can cause earlier boundary layer separation, which can disrupt the smooth flow of air over the wings and lead to a reduction of lift. This can cause the aircraft to stall at a lower angle of attack, increasing the risk of a dangerous situation for the pilot and passengers as it influences the control of the aircraft [11].

By improving the accuracy of CFD methods in modelling surface roughness, designers and manufacturers can better understand the effects of roughness on an aircraft's stall behaviour and make informed decisions about how to optimize the design of the aircraft's wings and other surfaces.

1.4 Research Objectives

The main objective of this research is to model the surface roughness to compare its simulated effect on aircraft stall with experimental data. The project has some restrictions to follow. The model is to be implemented in the unstructured finite volumes compressible RANS code CHAMPS, developed at Polytechnique Montréal [12]. Therefore, the project requires the use and implementation of turbulence and transition models and needs to be coded in the programming language Chapel. The following is the proposed sub-objective(SO):

1. Examine the behaviour of the two most popular turbulence models ($SO1$)
2. Introduce transition effects ($SO2$)
3. Examine the effect of roughness ($SO3$)

For the sub-objective 1, the Spalart-Allmaras turbulence model [13] is already implemented in CHAMPS. Therefore, $SO1$ requires implementing the $k-\omega$ turbulence model from Menter [14].

The sub-objective 2 is achieved by implementing the γ-$\tilde{Re}_{\theta t}$ transition model which is coupled with the $k-\omega$ turbulence model. Moreover, $SO2$ also requires to couple the transition model with the Spalart-Allmaras turbulence as some researcher have shown that there is numerical advantages for such combination. It is also relevant to compare the results of the two turbulence model for the transition. Finally, $SO2$ is completed with the addition of a crossflow extension to take into account the crossflow-induced transition that occurs in 3D.

The sub-objective 3 is satisfied by adding the roughness effect to the transition models with a transport equation and modification to the wall boundary condition. This allows the effect of the roughness to be transported by the flux. $SO3$ examines the stall characteristics of the simulations with the roughness with experimental data.

1.5 Thesis Outline

Chapter 2 presents the literature review of the turbulence models used in this thesis and some of the alternative methods. Chapter 3 presents the methodology used for the implementation of the turbulence, transition and roughness models. The results of the transition are shown in Chapter 4 along with an investigation to understand the cause of early natural transition in which a solution is proposed. Chapter 5 focuses on the results using the roughness model and the effect on the drag and lift curves and stall performance. The thesis ends in Chapter 6 with the conclusion along the recommendations, limitations and future work.

CHAPTER 2 LITERATURE REVIEW

This chapter presents an overview of the alternative approaches found in the literature to model the turbulence and the effect of surface roughness. The different Computational Fluid Dynamic (CFD) methods are first described in Section 2.1, focusing on the Reynold-Average-Navier-Stoke (RANS) and the intermittency and vorticity Reynold number methods, often referred to as the γ-$\tilde{Re}_{\theta t}$ transition model. The γ-$\tilde{Re}_{\theta t}$ model is reviewed in more depth in Section 2.2. Finally, the chapter ends by discussing the roughness models in Section 2.3.

2.1 CFD Methods Used for Turbulence Modelling

Turbulence is difficult to model since this phenomenon has many characteristics that increase the complexity. In the literature, Ferziger and al. [15] list some important characteristics of the turbulence:

- It is **unsteady**. The velocity profile for a giving point in space may change with time.
- It has **vorticity**. The particles in a turbulent flow have the tendency of moving in rotation. The turbulence intensity is increased by the growth of vorticity [15]. Therefore, it is an important property of the flow that is used in many turbulence models.
- It is **diffusive**. The mixing of the flow increase the contacts of the particles of different concentrations of the conserved properties, therefore, increasing the stirring of these properties [15]. For example, heat will spread faster in a turbulent flow.
- It is **dissipative**. Due to the viscosity and the mixing of the fluid, there is a loss of the kinetic energy of the flow which is irreversibly converted to internal energy [15].
- It has **different scales**. Turbulence can happen at very small length and time periods, but also large length and time periods [15].

Therefore, the existing available methods are limited to only the ones that can simulate such complex phenomena. The following methods are some of the popular approach used in the literature.

2.1.1 Direct Numerical Simulation (DNS)

The most accurate method is to directly solve the Navier-Stokes equations which are a set of 5 differential transport equations that describe the behaviour of the fluids. These equations correspond to the conservation laws:

1. the conservation of mass (1 equation)
2. the conservation of momentum (3 equations in 3D)
3. the conservation of energy (1 equation)

DNS can simulate the transition very accurately. However it requires very fine grids to be able to simulate the small-scale turbulence [16]. This requirement leads to expensive computational resources and therefore is not suitable for industrial applications.

2.1.2 Large Eddy Simulation (LES)

Another model to simulate the turbulence is LES, first proposed by Smagorinsky [17] in 1963. The idea behind this method is to solve for the large eddy only and ignore the small-scale turbulence in order to reduce computational cost. The transition prediction was initially sensitive to the Smagorinsky constant. Therefore, to take into account the effect of the small eddies and reduce this sensitivity, a SubGrid scale (SGS) model eddy viscosity approach was developed by Germano and al. [18] in 1991. This approach requires less computational cost than DNS, but is also less accurate. However, the computational cost remains very high for industrial applications.

2.1.3 Reynold-Average Navier-Stokes (RANS)

RANS also aims to solve the Navier-Stoke system of equations, but uses the Reynolds decomposition to average these equations. By averaging the system, a Reynolds stress appears. One way to close the problem is to use an eddy viscosity model for the turbulence. Therefore, very fine mesh is not a requirement as much as it is with DNS to simulate the turbulence. Such an approach has the benefit of having acceptable computational cost for industrial applications, but the drawback is less accuracy compared to DNS and additional equations are needed to solve for the turbulent eddy viscosity. In comparison, LES has the potential to be more accurate than RANS simulations, but it is also more time consuming [19]. It is possible

to consider the RANS model sufficient when applying the best practices [19]. Two of the popular turbulence models used along RANS in aerospace applications are the one equation Spalart-Allmaras turbulence model [13] and the two equations Menter $k-\omega$ SST turbulence model [14]. These models are introduced with more details in Chapter 3.

In the literature, there are different approaches to simulate the transition using the RANS model. The following are some of the methods which are further described and compared in the work of Pasquale and al. [16]:

- Stability theory approach (e^n method)
- Low Reynold number turbulent closure approach
- Intermittency transport method with empirical correlations
- Laminar fluctuation energy method
- $\bar{\nu^2} - f$ model
- Intermittency and vorticity Reynold number approach

The intermittency and vorticity Reynold number approach, referred to as the γ-$\tilde{R}e_{\theta t}$ transition model, is the imposed method for this project. Although the alternative methods have their advantages and disadvantages, some would have been rejected for obvious reasons. For example, the stability theory is not an ideal approach as it cannot predict the non-linear effect of high freestream turbulence and surface roughness [16] which are important effects for this study. Finally, the Low Reynold number approach is only ideal to predict by-pass transition [16].

2.2 The γ-$\tilde{R}e_{\theta t}$ transition model

The γ-$\tilde{R}e_{\theta t}$ transition model was developed by Langtry and Menter [9] [20]. The idea is to simulate the different transition mechanisms using the concept of intermittency and local values determined by correlations. Such an approach is commonly referred to as Local Correlation-Based Transition Model (LCTM) [21]. The intermittency is a measure of the probability of the local cell to be in a turbulent region [9]. Its range is 0 (laminar) to 1 (turbulent). The first transport equation is for the intermittency (γ) and its value controls the production of turbulence in the boundary layer. The second transport equation solves for

the transition momentum thickness Reynold number ($\tilde{Re}_{\theta t}$), used to provide local quantities from the experimental correlation. Since a turbulence model is needed, the authors originally coupled the model with the $k-\omega$ SST turbulence model [14]. Later, Medina and Baeder [22] have coupled it with the Spalart-Allmaras (SA) [13] turbulence model.

2.3 Roughness effect

There are different approaches in the literature to simulate the roughness. The ideal approach would be to use an ultra-fine mesh size to model the geometry of the roughness elements. However it would not be computationally realistic. Another approach is to modify the transport equations to take into account the effect of momentum loss due to the increase of the surface drag [23]. This method presents some advantages, however the results are very sensitive to small errors [23]. The most popular approach is to modify the near-wall eddy viscosity according to the height of the roughness [23]. An extension for the $k-\omega$ SST turbulence model was developed using this approach in the work of Hellsten and Laine [24] in 1997. The $k-\epsilon$ turbulence model was also modified for the roughness in the work of Durbin and al. [25] in 2000. Later in 2003, Aupoix and Spalart [26] developed a roughness extension for the popular Spalart-Allmaras turbulence model [13].

These modifications change the wall boundary condition of the turbulence models. However, in the laminar boundary layer, the effect of the roughness on the transition is not well represented since the boundary condition for the rough wall has a local effect only. To improve the models, Dassler, Kozulovic and Fiala [27] introduced a new transport equation to add to the Langtry and Menter transition model [20]. The equation is solved for the Roughness Amplification (A_r) variable which is a non-physical quantity produced at the rough wall boundary condition. The convective flux from this transport equation allows taking into account the influence of the roughness to the flow field. Then, the variable A_r locally modifies the transition model and therefore the transition onset.

CHAPTER 3 METHODOLOGY

This chapter presents the methodology developed in order to achieve the goals of this thesis. Mainly, how the models were implemented in the code and the different strategies used. Section 3.1 and 3.2 described the equations of the turbulence models that were implemented. The reader is referred to the original references for a complete description of the turbulence models. Section 3.3 presents with more focus the γ-$\tilde{Re}_{\theta t}$ transition model that is coupled with the two turbulence models, as it is an important part of the methodology. Section 3.4 presents the equations of the crossflow extension which were added to simulate the crossflow-induced transition. Section 3.5 describes the roughness model and equations that were implemented to add the effect of the surface roughness. Finally, Section 3.6 presents the RANS software CHAMPS that was used to implement the models. Note that for compactness, the $k-\omega$, $k-\epsilon$ and $k-\omega$-γ-$\tilde{Re}_{\theta t}$ models are sometimes referred to as the kω, kϵ and kω-γ-$\tilde{Re}_{\theta t}$ models throughout the document. Note that parts of this chapter are based on the reference of Bilodeau-Bérubé and al. [28].

3.1 Spalart-Allmaras Turbulence Model

The Spalart and Allmaras (SA) turbulence model was developed in 1992 [13]. Instead of solving ν_t directly, the model solves $\tilde{\nu}$ using one transport equation:

$$\frac{\partial \tilde{\nu}}{\partial t} + u_j \frac{\partial \tilde{\nu}}{\partial x_j} = P_{\tilde{\nu}} - D_{\tilde{\nu}} + \frac{1}{\sigma}\left[\frac{\partial}{\partial x_j}\left[(\nu+\tilde{\nu})\frac{\partial \tilde{\nu}}{\partial x_j}\right] + c_{b2}\frac{\partial \tilde{\nu}}{\partial x_j}\frac{\partial \tilde{\nu}}{\partial x_j}\right] \tag{3.1}$$

$$P_{\tilde{\nu}} = c_{b1}(1-f_{t2})\tilde{S}\tilde{\nu} \tag{3.2}$$

$$D_{\tilde{\nu}} = \left[c_{w1}f_w - \frac{c_{b1}}{\kappa^2}f_{t2}\right]\left(\frac{\tilde{\nu}}{d}\right)^2 \tag{3.3}$$

The eddy viscosity is then computed with the following:

$$\nu_t = \tilde{\nu} f_{\nu 1} \tag{3.4}$$

$$f_{\nu 1} = \frac{\chi^3}{\chi^3 + C_{\nu 1}^3} \tag{3.5}$$

$$\chi = \frac{\tilde{\nu}}{\nu_t} \tag{3.6}$$

where c_{b1}, c_{w1}, c_{b2} and κ are constants, $f_{\nu 1}$, f_w and f_{t2} are functions defined in [13].
The boundary conditions are the following:

$$\tilde{\nu}_{wall} = 0, \quad \tilde{\nu}_{farfield} = 3\tilde{\nu}_\infty : to : 5\tilde{\nu}_\infty \tag{3.7}$$

3.2 $k-\omega$ SST Turbulence Model

The $k-\omega$ SST model was developed by Menter in 1994 [14] in order to overcome the original $k-\omega$ dependency on the freestream turbulence conditions while maintaining its advantage near walls when there is an adverse pressure gradient. To do so, the model uses a blending function to switch from the $k-\epsilon$ model in the freestream to the $k-\omega$ model when approaching a wall. The model is composed of two transport equations to solve the eddy viscosity comparatively to one for the SA model. The first one is for the kinetic energy (k) and the second is for the specific turbulence dissipation rate (ω):

$$\frac{\partial(\rho k)}{\partial t} + \frac{\partial(\rho u_j k)}{\partial x_j} - \frac{\partial}{\partial x_j}\left[(\mu + \sigma_k \mu_t)\frac{\partial k}{\partial x_j}\right] = P_k - D_k \tag{3.8}$$

$$\frac{\partial(\rho \omega)}{\partial t} + \frac{\partial(\rho u_j \omega)}{\partial x_j} - \frac{\partial}{\partial x_j}\left[(\mu + \sigma_\omega \mu_t)\frac{\partial \omega}{\partial x_j}\right] = \frac{\gamma}{\nu_t}P_k - D_\omega \tag{3.9}$$

$$D_k = \beta^* \rho \omega k \tag{3.10}$$

$$D_\omega = \beta \rho \omega^2 + 2(1-F_1)\frac{\rho \sigma_{\omega 2}}{\omega}\frac{\partial k}{\partial x_j}\frac{\partial \omega}{\partial x_j} \tag{3.11}$$

The eddy viscosity is then computed with the following:

$$\nu_t = \frac{\rho a_1 k}{max(a_1 \omega, \Omega F_2)} \tag{3.12}$$

where σ_k, σ_ω, $\sigma_{\omega 2}$, a_1, β and β^* are constant, $f_{\nu 1}$, F_1, F_2 and γ are functions defined in [14].

When ν_t reaches 0.0, it causes numerical difficulties. The solution is to use a limiter in the update:

$$\nu_t = max(\nu_t, 10^{-12}\nu_{t,\infty}) \tag{3.13}$$

The boundary conditions, when coupled with γ-$\tilde{Re}_{\theta t}$ equations, are as follows:

$$k_{wall} = 0, \quad \omega_{wall} = 60\frac{\nu}{\beta_1 d^2} \tag{3.14}$$

$$k_{farfield} = \frac{3}{2}\left(TuU\right)^2, \quad \omega_{farfield} = \frac{\rho k}{\mu_t} \tag{3.15}$$

with β_1 a model constant defined in [14], and Tu the local turbulence intensity which is further discussed in Section 3.3.1.

The basic form of the equations has the problem of turbulence decay in the freestream. To prevent the decay, the following correction can be used in the implementation [29]:

$$P_k = P_k + \beta^* \rho \omega_{amb} k_{amb} \tag{3.16}$$

$$P_\omega = P_\omega + \beta \rho \omega_{amb}^2 \tag{3.17}$$

$$\omega_{amb} = \frac{5U_\infty}{L} \tag{3.18}$$

$$k_{amb} = 10^{-6} U_\infty^2 \tag{3.19}$$

3.3 γ-$\tilde{Re}_{\theta t}$ Transition Model

The transport equations for the intermittency γ and the momentum thickness Reynold number $\tilde{Re}_{\theta t}$ are the following:

$$\frac{\partial \gamma}{\partial t} + u_j \frac{\partial \gamma}{\partial x_j} = P_\gamma - E_\gamma + \frac{\partial}{\partial x_j}\left[\left(\mu + \frac{\mu_t}{\sigma_f}\right)\frac{\partial \gamma}{\partial x_j}\right] \tag{3.20}$$

$$\frac{\partial \tilde{Re}_{\theta_t}}{\partial t} + u_j \frac{\partial \tilde{Re}_{\theta t}}{\partial x_j} = P_{\theta_t} + D_{cf} + \frac{\partial}{\partial x_j}\left[\sigma_{\theta t}\left(\mu + \mu_t\right)\frac{\partial \tilde{Re}_{\theta t}}{\partial x_j}\right] \tag{3.21}$$

$$P_\gamma = F_{length} c_{a1} S \sqrt{\gamma F_{onset}} \rho (1 - c_{e1}\gamma) \tag{3.22}$$

$$E_\gamma = c_{a2} \Omega F_{turb} \rho \gamma (c_{e2}\gamma - 1) \tag{3.23}$$

$$P_{\theta_t} = \rho \frac{c_{\theta_t}}{t}(1 - F_{\theta_t})(Re_{\theta_t} - \tilde{Re}_{\theta_t}) \tag{3.24}$$

$$t = \frac{500\mu}{\rho U^2} \tag{3.25}$$

$$F_{\theta_t} = F_{wake} e^{-(d/\delta)^4}, \quad F_{wake} = e^{-Re_S/10^6}, \quad Re_S = \frac{\rho d^2 S}{\mu} \tag{3.26}$$

$$\delta = \frac{50d\Omega}{U}\delta_{BL}, \quad \delta_{BL} = \frac{15}{2}\frac{\tilde{R}e_{\theta t}\mu}{\rho U} \tag{3.27}$$

$$c_{a1} = 2.0, \quad c_{a2} = 0.06, \quad c_{e1} = 1.0, \quad c_{e2} = 50, \quad \sigma_{\theta t} = 2.0, \quad \sigma_f = 1 \tag{3.28}$$

where F_{onset}, F_{length} and Re_{θ_t} are correlation-based functions defined below.

The boundary conditions are the following, as given in [20]:

$$\frac{\partial \gamma}{\partial n}|_{wall} = 0, \quad \gamma_{farfield} = 1 \tag{3.29}$$

$$\frac{\partial \tilde{R}e_{\theta_t}}{\partial n}|_{wall} = 0, \quad \tilde{R}e_{\theta t, farfield} = \begin{cases} (1173.51 - 589.428Tu_\infty + 0.2196Tu_\infty^{-2}) & \text{if} \quad Tu_\infty \leq 1.3, \\ 331.50(Tu_\infty - 0.5658)^{-0.671} & \text{if} \quad Tu_\infty > 1.3 \end{cases} \tag{3.30}$$

The transition model is referred to as the SA-γ-$\tilde{R}e_{\theta t}$ when coupled with the SA turbulence model, and $k\omega$-γ-$\tilde{R}e_{\theta t}$ when coupled with the $k-\omega$ SST turbulence model.

3.3.1 Turbulence intensity

The turbulence intensity Tu is an important input in transition models. Its initial value can affect the location of the transition. In experiments, the freestream value of Tu, Tu_∞, is often measured. The local value of Tu is defined as follows:

$$Tu = 100\frac{\sqrt{2k/3}}{U} \tag{3.31}$$

where k is the turbulent kinetic energy and U is the local flow velocity. When the intermittency, γ, decreases in the laminar boundary layer, it can sometimes cause a decrease in the local value of k. This is because the production term of the k equation is multiplied by γ_{eff} in the k-coupling equation. Since Tu is strongly dependent on the value of k, the value of Tu will therefore decrease in the laminar region before transition. In addition, its local value can also decay in the freestream and have a lower value at the geometry. Several strategies can be used to address this, such as using a control decay correction, but the simplest solution is to choose a higher freestream value for Tu_∞.

In contrast, the SA-γ-$\tilde{R}e_{\theta t}$ model does not include the variable k and Tu is kept constant at Tu_∞, as proposed by Medida et al. [22]. This makes calibration more challenging when

comparing the two models, since the selected value for Tu_∞ will affect them differently. To account for this, the value selected for the $k\omega$-γ-$\tilde{R}e_{\theta t}$ model should be equal to or greater than the one selected for the SA-γ-$\tilde{R}e_{\theta t}$ model, so that their local values are more similar inside the laminar boundary layer. Note that this is a trial-and-error process and the values are not always chosen so that both models produce identical results.

3.3.2 Transition criteria

Since the transition from laminar to turbulent flow can be characterized by a sharp rise of the friction drag C_f, the transition can be visualized using C_f along the streamwise direction which is the x axis for this example. The following is a simple criterion that returns the location based on the position of the maximum slope of this curve:

$$x_{tr}\left(x\right) = x\big|_{max\left(dC_f(x)/dx\right)} \tag{3.32}$$

The criteria return the transition location about in the middle of the transition region. Therefore, it has the disadvantage of giving values a bit too far downstream, especially when the transition region extends over more distance.

Another approach is to use the turbulence index (i_t) from the work of Spalart and Allmaras [13]:

$$i_t = \frac{1}{\kappa\mu_\tau}\frac{\partial\tilde{\nu}}{\partial n} \tag{3.33}$$

Using this approach, the flow is considered laminar when $i_t = 0$ and turbulent when $i_t = 1$. The transition location is returned when i_t exceeds 1, which is usually about the beginning of the increase of C_f. It has the disadvantage of returning multiple false transition locations, and the true ones can sometimes be a bit too early. Note that this criterion was implemented in the latest part of this project, therefore the criteria from Eq. (3.32) has been used.

3.3.3 Re_{θ_t} Correlation and Resolution

The transition onset Momentum thickness Reynolds number (Re_{θ_t}) correlation for natural and bypass transition is the following [20]:

$$Re_{\theta_t} = \frac{\rho U \theta_t}{\mu} = \begin{cases} [1173.51 - 589.428Tu + 0.2196/Tu^2]F(\lambda_{\theta_t}) & \text{if} \quad Tu \leq 1.3, \\ 331.5[Tu - 0.5658]^{-0.671}F(\lambda_{\theta_t}) & \text{if} \quad Tu > 1.3 \end{cases} \tag{3.34}$$

$$F(\lambda_{\theta_t}) = \begin{cases} 1 - [-12.986\lambda_{\theta_t} - 123.66\lambda_{\theta_t}^2 - 405.689\lambda_{\theta_t}^3]e^{\frac{Tu}{1.5})^{1.5}} & \text{if} \quad \lambda_{\theta_t} \leq 0.0, \\ 1 + 0.275[1 - e^{-35\lambda_{\theta_t}}]e^{-2Tu} & \text{if} \quad \lambda_{\theta_t} > 0.0 \end{cases} \tag{3.35}$$

The equation is implicit for θ_t since the variable cannot be isolated and directly solved. Therefore, the Newton method is proposed with an iterative loop over the variable θ_t. The Newton function $f(\theta_t)$ is created and should tend to zero when the method converges to the correct value of θ_t. The derivative $f\prime(\theta_t)$ is also needed for the Newton method:

$$f(\theta_t) = 0 = \begin{cases} [1173.51 - 589.428Tu + 0.2196/Tu^2]F(\lambda_{\theta_t}) - \frac{\rho U \theta_t}{\mu} & \text{if} \quad Tu \leq 1.3, \\ 331.5[Tu - 0.5658]^{-0.671}F(\lambda_{\theta_t}) - \frac{\rho U \theta_t}{\mu} & \text{if} \quad Tu > 1.3 \end{cases} \tag{3.36}$$

$$f\prime(\theta_t) = \begin{cases} [1173.51 - 589.428Tu + 0.2196/Tu^2]F\prime(\lambda_{\theta_t}) - \frac{\rho U}{\mu} & \text{if} \quad Tu \leq 1.3, \\ 331.5[Tu - 0.5658]^{-0.671}F\prime(\lambda_{\theta_t}) - \frac{\rho U}{\mu} & \text{if} \quad Tu > 1.3 \end{cases} \tag{3.37}$$

$$F\prime(\lambda_{\theta_t}) = \begin{cases} [12.986 + 247.32\lambda_{\theta_t} + 1217.067\lambda_{\theta_t}^2]e^{\frac{Tu}{1.5})^{1.5}} \frac{d\lambda_{\theta_t}}{d\theta_t} & \text{if} \quad \lambda_{\theta_t} \leq 0.0, \\ 9.625e^{-35\lambda_{\theta_t}}e^{-2Tu}\frac{d\lambda_{\theta_t}}{d\theta_t} & \text{if} \quad \lambda_{\theta_t} > 0.0 \end{cases} \tag{3.38}$$

$$\frac{d\lambda_{\theta_t}}{d\theta_t} = \frac{2\rho\theta_t}{\mu}\frac{dU}{ds} \tag{3.39}$$

An initial guess for $\theta_{t,k}$ must be given and the next value at iteration $k+1$ is obtained with the following equation:

$$\theta_{t,k+1} = \theta_{t,k} - \frac{f(\theta_{t,k})}{f\prime(\theta_{t,k})} \tag{3.40}$$

In the literature [9], the initial guess for the local value of θ_t is usually obtained based on the zero pressure gradient solution $F(\lambda_{\theta_t} = 0) = 1$. However, up to $10 - 15$ iterations can be required to get a satisfactory error under 10^{-10}. This leads to a higher computational time as this iterative loop must be repeated for every cell and for every iteration of the flow and turbulence solvers.

An improvement is thus proposed: at the initialization of the solver before the first iteration of the RANS model, the zero pressure gradient solution is used as a first guest for θ_t like

in the literature. But afterwards, the converged value of θ_t of each cell is passed to be the initial guest for the next iteration of the flow and turbulence solvers. With this change, the number of iterations of the Newton method rapidly reduces to only 1-2 iterations per cell to obtain an error under 10^{-14}, reducing the computational cost.

3.3.4 F_{length} and Re_{θ_c} Correlations

The F_{length} function acts on the length of the transition process in Eq. (3.22). Higher values of F_{length} will increase the production of the intermittency and the flow will become turbulent over a shorter length. The original correlation from Langtry [9] is the following:

$$F_{length} = \begin{cases} 39.8189 - 119.270 \times 10^{-4}\tilde{R}e_{\theta_t} - 132.567 \times 10^{-6}\tilde{R}e_{\theta_t}^2 & \text{if} \quad \tilde{R}e_{\theta_t} < 400 \\ 263.404 - 123.939 \times 10^{-2}\tilde{R}e_{\theta_t} + 194.548 \times 10^{-5}\tilde{R}e_{\theta_t}^2 & \\ -101.695 \times 10^{-8}\tilde{R}e_{\theta_t}^3 & \text{else if} \quad \tilde{R}e_{\theta_t} < 596 \\ 0.5 - (\tilde{R}e_{\theta_t} - 596.0)3.0 \times 10^{-4} & \text{else if} \quad \tilde{R}e_{\theta_t} < 1200 \\ 0.3188 & \text{else} \end{cases} \tag{3.41}$$

The critical Reynold number Re_{θ_c} is also calculated using a correlation with the following from Langtry [9]:

$$Re_{\theta_c} = \begin{cases} \tilde{R}e_{\theta_t} - (396.035 \times 10^{-2} - 120.656 \times 10^{-4}\tilde{R}e_{\theta_t} & \\ +868.230 \times 10^{-6}\tilde{R}e_{\theta_t}^2 - 696.506 \times 10^{-9}\tilde{R}e_{\theta_t}^3 + 174.105 \times 10^{-12}\tilde{R}e_{\theta_t}^4) & \text{if} \quad \tilde{R}e_{\theta_t} \leq 1870 \\ \tilde{R}e_{\theta_t} - (593.11 + 0.482(\tilde{R}e_{\theta_t} - 1870.0)) & \text{else} \end{cases} \tag{3.42}$$

Both correlations have discontinuities created by the *if else*. In the literature, Piotrowski and Zingg [2] chose to modify these correlations to improve their smoothness and to improve the residual convergence of their solver. The following equations are the modified correlations:

$$Re_{\theta_c} = 0.67\tilde{R}e_{\theta_t} + 24\sin\left(\frac{\tilde{R}e_{\theta_t}}{240} + 0.5\right) + 14 \tag{3.43}$$

$$F_{length1} = \exp\left(-3 * 10^{-2}(\tilde{R}e_{\theta_t} - 460)\right) \tag{3.44}$$

$$F_{length} = 44 - \frac{44 - (0.50 - 3 * 10^{-4}(\tilde{R}e_{\theta_t} - 596))}{(1 + F_{length1})^{\frac{1}{6}}} \tag{3.45}$$

The original and the smooth correlations are compared in Figure 3.1. It can be observed that the smooth correlations have their outputs almost unchanged compared to the original ones.

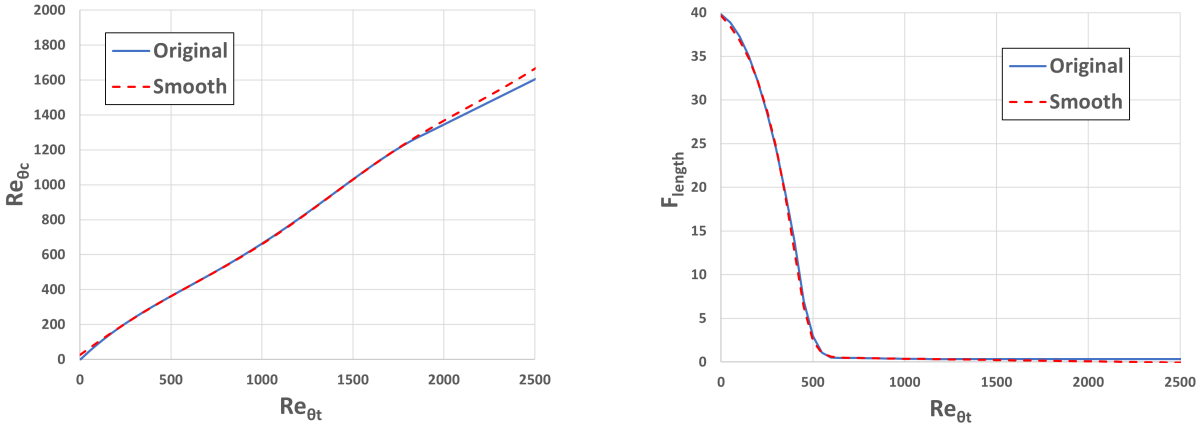

(a) $R_{e\theta_c}$ (b) F_{length}

Figure 3.1 Piotrowski & Zingg smooth correlations [2] for F_{length} and Re_{θ_c} compared to the original equations

Simulations with and without the smooth correlations were carried out on the NLF0416 airfoil case with an extra fine grid resolution of size 2049×513. The comparison of the residual convergence is displayed on Figure 3.2. It shows very little differences in the residual convergence between the original and smoothed correlations. The smooth correlations also did not affect the solution of the transition. This could be because they were designed to improve the residual convergence for a fully coupled and fully implicit Newton-Krylov solver [2] which is more sensitive to non-differentiable terms than the Block SGS scheme used in CHAMPS.

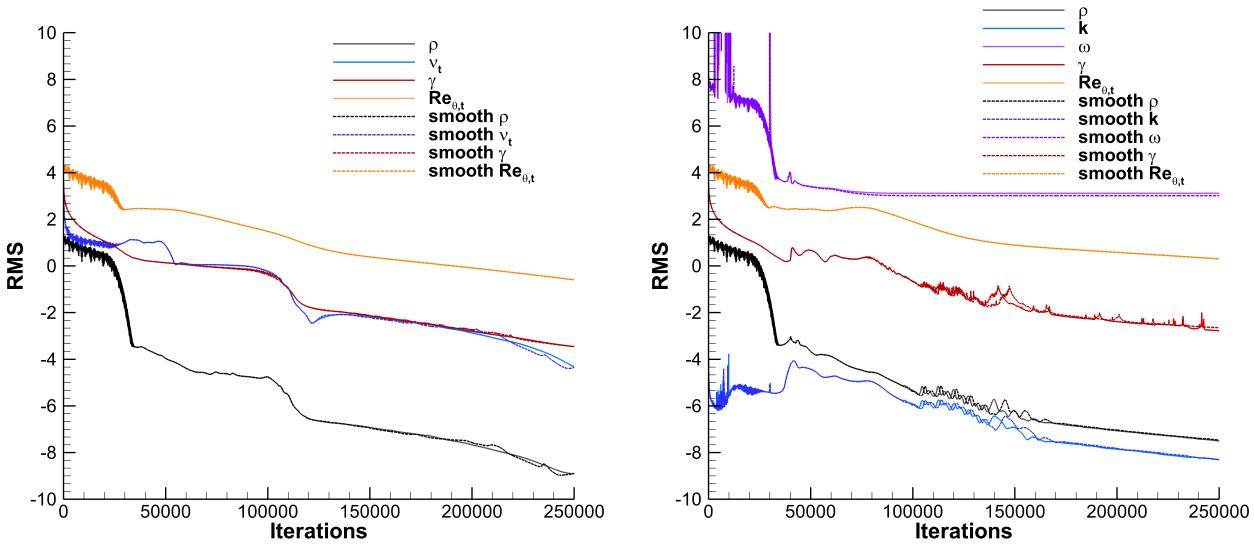

(a) SA-$\tilde{R}e_{\theta t}$ model

(b) $k\omega$-γ-$\tilde{R}e_{\theta t}$ model

Figure 3.2 Effect of the Piotrowski & Zingg smooth correlations on the residual convergence for the NLF0416 case ($grid = 2049 \times 513, M = 0.10, Re = 4 \times 10^6, Tu_\infty = 0.15\%, AoA = 0°$) compared to the original correlations

3.3.5 Investigation of the F_{onset} parameters

The F_{onset} function in Eq. (3.22) is used to trigger the intermittency production. The variables in play are the local vorticity Reynold number Re_v and the critical Reynold number Re_{θ_c} on which is based F_{onset1} in Eq. (3.46). F_{onset1} acts as a transition criterion in F_{onset} [9]. When this transition criterion exceeds 1.0, then F_{onset} is rapidly activated as can be seen in Figure 3.3. Another important variable is the viscosity ratio (RT) used in F_{onset3} from Eq. (3.48). According to Langtry [9], the main purpose of RT is to allow F_{onset} to remain active when the vorticity starts decreasing in the transition process.

$$F_{onset1} = \frac{Re_\nu}{2.193 Re_{\theta c}} \tag{3.46}$$

$$F_{onset2} = min(max(F_{onset1}, F_{onset1}^4), c_{opt4}) \tag{3.47}$$

$$F_{onset3} = max(c_{opt1} - \frac{1}{2.5^3} RT^3, 0) \tag{3.48}$$

$$F_{onset} = max(F_{onset2} - F_{onset3}, 0) \tag{3.49}$$

Piotrowski and Zingg [21] and Barouillet and al. [30] calibrated their models by changing the

value of two parameters $\{c_{opt1}, c_{opt4}\}$ in the F_{onset} equations. By default, these constants are set to $\{1, 2\}$ in the original model. But in their work, the former fixed the values at $\{2, 4\}$ and the latter at $\{2, 2\}$. As it can be seen in Fig. 3.3b, the use of $\{2, 2\}$ is the only option that does not allow the production of intermittency when RT is too low. Therefore, the calibration with $\{2, 2\}$ may not always allow F_{onset} to work as intended in the original model since the transition would only be triggered when RT increases and not when the transition criterion is met. Results of the investigation can be found in Section 4.1.3. Note that the original values of $\{1, 2\}$ were selected by default in this work for all simulations.

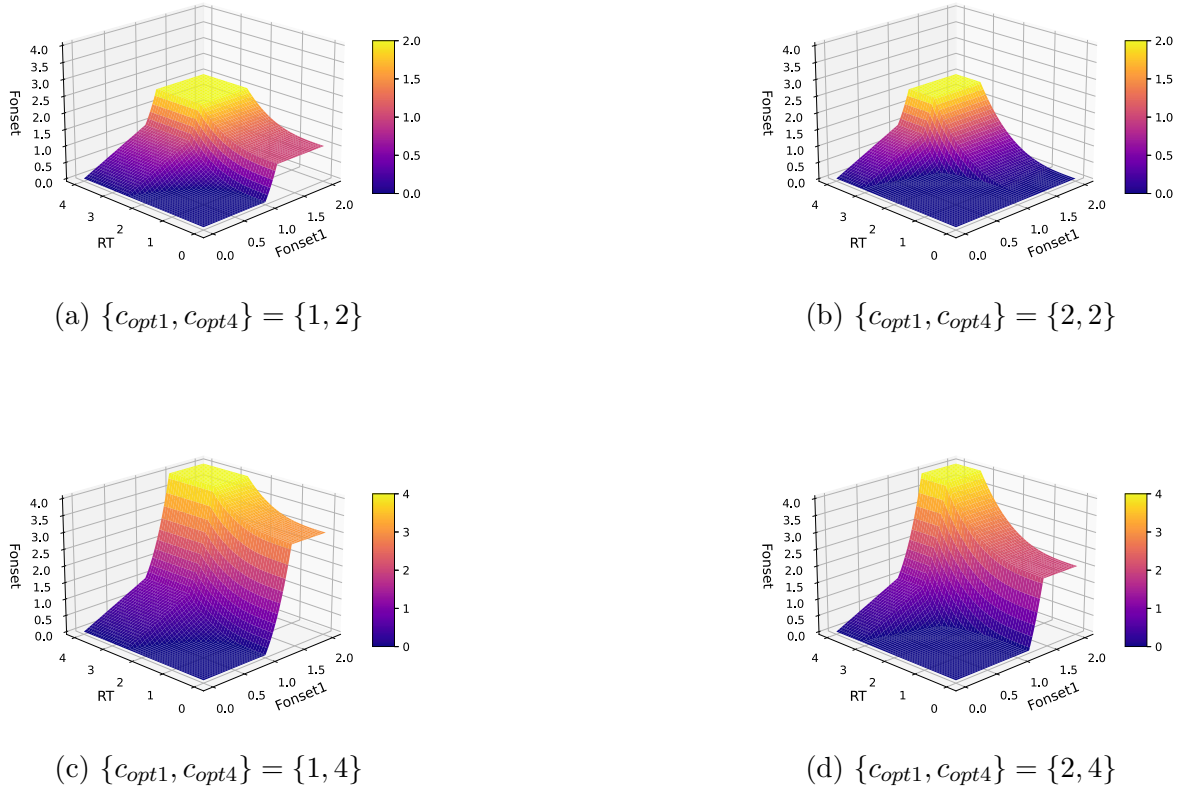

(a) $\{c_{opt1}, c_{opt4}\} = \{1, 2\}$

(b) $\{c_{opt1}, c_{opt4}\} = \{2, 2\}$

(c) $\{c_{opt1}, c_{opt4}\} = \{1, 4\}$

(d) $\{c_{opt1}, c_{opt4}\} = \{2, 4\}$

Figure 3.3 Influence of the parameters c_{opt1} and c_{opt4} on original F_{onset}

3.3.6 Residual convergence comparison and smoothing

Figure 3.4 displays a comparison of the SA-γ-$\tilde{Re}_{\theta t}$ and the $k\omega$-γ-$\tilde{Re}_{\theta t}$ models residual convergence. The NLF0416 airfoil is used with an extra fine grid resolution of size 2049×513 and the two simulations have the same parameters. The SA-γ-$\tilde{Re}_{\theta t}$ model performed better than the $k\omega$-γ-$\tilde{Re}_{\theta t}$ model with a smoother convergence, as expected. The $k\omega$-γ-$\tilde{Re}_{\theta t}$ model has

intense oscillations at the beginning of the ω residual. Oscillations seen with the ω residual often occurred throughout the simulations and when they are more severe, it can sometimes cause the simulations to fail or limit the maximum allowable time step.

Barouillet and al. [30] introduced a smoothing for the F_{onset} equation which consists of smoothing the discontinuity created by the *max* function of the F_{onset} equation (3.49) when it approaches zero:

$$f_{o23} = F_{onset2} - F_{onset3} \tag{3.50}$$

$$F_{onset} = \begin{cases} f_{o23}, & \text{if } f_{o23} > c_{opt3} \\ exp(\frac{f_{o23}-c_{opt3}}{c_{opt3}} c_{opt3}), & \text{otherwise, } c_{opt3} \in [10^{-5}, 10^{-1}] \end{cases} \tag{3.51}$$

The residual convergences, with and without this smoothing, are compared in Figure 3.4. In their work, Barouillet and al. showed that it can significantly improve the convergence. However, Figure 3.4 shows very little differences in the residual convergence between the original and smoothed equation, except for the γ residual of the $k\omega$-γ-$\tilde{Re}_{\theta t}$ model. This behaviour is contrary to what was observed by Barouillet et al. in [30]. Even so, note that in few other cases with the $k\omega$-γ-$\tilde{Re}_{\theta t}$ model, it was observed that the smoothing could sometimes help with the robustness. For this reason, smoothing was chosen if needed for some simulations presented in this document.

3.3.7 Models Coupling

The turbulence model and the γ-$\tilde{Re}_{\theta t}$ transition model are coupled through the local value of the effective intermittency γ_{eff}:

For the $k-\omega$ based model:

$$\tilde{P}_k = \gamma_{eff} P_k \tag{3.52}$$

$$\tilde{D}_k = min(max(\gamma_{eff}, \beta), 1) D_k \tag{3.53}$$

For the SA based model:

$$\tilde{P}_{\tilde{\nu}} = \gamma_{eff} P_{\tilde{\nu}} \tag{3.54}$$

$$\tilde{D}_{\tilde{\nu}} = min(max(\gamma_{eff}, \beta), 1) D_{\tilde{\nu}} \tag{3.55}$$

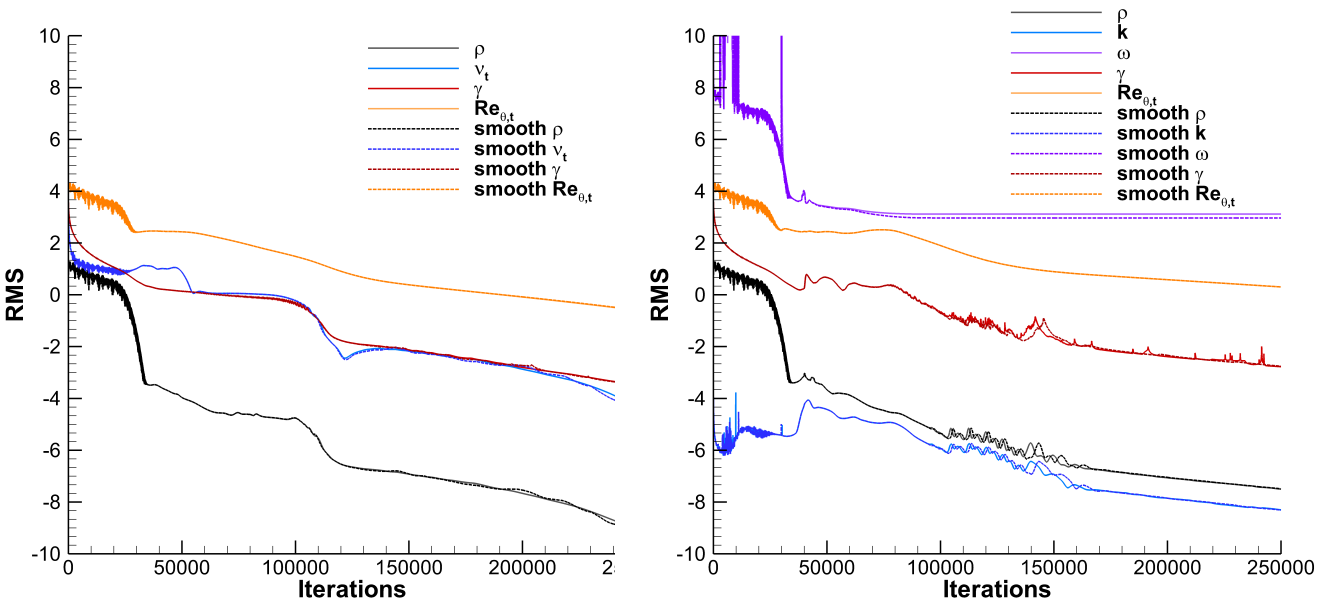

(a) SA-$\tilde{Re}_{\theta t}$ model (b) $k\omega$-γ-$\tilde{Re}_{\theta t}$ model

Figure 3.4 Comparison of the residual convergence on the NLF0416 case and effect of the F_{onset} smoothing ($grid = 2049 \times 513, M = 0.10, Re = 4 \times 10^6, Tu_\infty = 0.15\%, AoA = 0°$)

The effective intermittency is defined as:

$$\gamma_{eff} = max(\gamma, \gamma_{sep}) \tag{3.56}$$

$$\gamma_{sep} = min(2max(0, \frac{Re_v}{3.235Re_{\theta,t}} - 1)e^{-\frac{RT}{20}^4}, 2)F_{\theta,t} \tag{3.57}$$

The effective intermittency was introduced by Langtry [9] as a separation-induced correction to improve the reattachment location that was too far downstream. This was due to the decrease of k when the boundary layer separates. The correction compensates by allowing the intermittency to exceed its maximum value of 1. According to Piotrowski and Zing [2], this correction is not needed for the SA-γ-$\tilde{Re}_{\theta t}$. However, it was initially decided to implement the separation-induced correction for SA-γ-$\tilde{Re}_{\theta t}$. Later in the project, personal experience with the model manifest that this correction is in fact useless with the SA-γ-$\tilde{Re}_{\theta t}$ model because γ_{eff} is always equivalent to γ in the transition region. For the $k\omega$-γ-$\tilde{Re}_{\theta t}$ model, disabling the correction often improves the smoothness of the residual convergence, but it can sometimes alter the solution in some cases.

In this context, the constant β defines the minimum value of the coupling with the destruction term. It is equal to 0.1 when coupled with the $k-\omega$ model as proposed in the original model [9]. It is equal to 0.5 when coupled with the SA model as recommended in the work of Medida and al. [22]. Note that in the work of Piotrowski and Zingg [21] in which they use the SA-γ-$\tilde{R}e_{\theta t}$ model, the value of 1.0 was used, but no explanation was given to justify this choice. This parameter influences the amount of skin friction after the transition. Therefore, it can be used for calibration purposed to adjust the height of the C_f curve like in the work of Medida and al. [22].

3.3.8 Variables Relaxation

The coupling between the turbulence and the transition model can cause numerical difficulties when the local value of the intermittency γ oscillates or converges too slowly or too fast. Mosahebi and Laurendeau [31] introduced relaxation in the update of the variable γ_{eff}. The following equation recalculated γ_{eff} by combining a percentage of the previous value with the new value:

$$\gamma_{eff}^{new} = \alpha\gamma_{eff}^{new} + (1-\alpha)\gamma_{eff}^{old} \tag{3.58}$$

where α is the relaxation coefficient [31] ranging from 1 (not relax) to 0 (fully relax) exclusively. In their work [31], they showed setting the value of $\alpha = 0.1$ improves the residual convergence performance. In this work, simulations with values close to $\alpha = 0.1$ have also manifest improvement with smoother convergence and the maximum possible time step can be sometime increased. Moreover, since γ_{eff} is strongly dependent on γ, it was chosen to under-relax γ instead of γ_{eff}. The reason is to relax all the terms under the influence of γ instead of just γ_{eff}.

For the implementation, it is more convenient to rewrite Eq. (3.58) as a function of the solution delta $\Delta\gamma$. The reason is that the delta of the conservatives variables $\Delta\vec{W}$ are outputs of the solver and the new values of the conservative variables $\vec{W}^{new}$ are computed with the following:

$$\vec{W}^{new} = \vec{W}^{old} + \Delta\vec{W} \tag{3.59}$$

This is achieved by substituting $\gamma^{new} - \gamma^{old} = \Delta\gamma$ in Eq. (3.58). The new formulation become:

$$\gamma^{new} = \gamma^{old} + \alpha\Delta\gamma \tag{3.60}$$

Note that the same is implemented for all the conservative variables by multiplying the delta

solutions with a relaxation coefficient:

$$\vec{W}^{new} = \vec{W}^{old} + \alpha_{\vec{W}} \Delta \vec{W} \tag{3.61}$$

3.4 Crossflow model for 3D applications

Transition due to crossflow instability mechanisms is a 3D only effect which is the main cause of transition on swept wing [32] and is very sensitive to the surface roughness. However, the original γ-$\tilde{Re}_{\theta t}$ transition model does not have the effects included. The effects are added by implementing the crossflow extension developed by Langtry and al. [32] in 2015. Note that the extension was originally designed for the $k\omega$-γ-$\tilde{Re}_{\theta t}$ model, but Piotrowski and Zingg [21] showed it can also be compatible with the SA-γ-$\tilde{Re}_{\theta t}$ model. For that reason, the extension was implemented and tested for both models.

This model follows the LCTM approach as only local values are used based on the measurement of the streamwise vorticity ($\Omega_{Streamwise}$) [32], also known as the helicity:

$$\Omega_{Streamwise} = \left| \vec{U} \cdot \vec{\Omega} \right| \tag{3.62}$$

with the unit velocity vector defines as:

$$\vec{U} = \left[\frac{u}{U}, \frac{v}{U}, \frac{w}{U} \right] \tag{3.63}$$

The local velocity magnitude is defined as:

$$U = \sqrt{u^2 + v^2 + w^2} \tag{3.64}$$

and the vorticity vector define as:

$$\vec{\Omega} = \left[\frac{\partial w}{\partial y} - \frac{\partial v}{\partial z}, \frac{\partial u}{\partial z} - \frac{\partial w}{\partial x}, \frac{\partial v}{\partial x} - \frac{\partial u}{\partial y} \right] \tag{3.65}$$

The nondimensionalized crossflow strength is measured with the following equation:

$$H_{crossflow} = \frac{\Omega_{Streamwise} d}{U} \tag{3.66}$$

A destruction term (D_{cf}) is added to the transport Eq. (3.21) of the $\tilde{R}e_{\theta t}$ transition model:

$$D_{cf} = c_{\theta t}\frac{\rho}{t}c_{crossflow}min(Re_{cf} - \tilde{R}e_{\theta t}, 0)F_{\theta t2} \tag{3.67}$$

$$F_{\theta t2} = min\left(F_{wake}e^{-(\frac{d}{\delta})^4}, 1\right) \tag{3.68}$$

$$c_{crossflow} = 0.6 \tag{3.69}$$

The following equations are the correlations that return the local value of Re_{cf}:

$$Re_{cf} = \frac{\rho(\frac{U}{0.82}}{\mu}\theta_t = -35.088ln\left(\frac{h}{\theta_t}\right) + 319.51 + f(+\Delta H_{crossflow}) - f(-\Delta H_{crossflow}) \tag{3.70}$$

$$\Delta H_{crossflow} = H_{crossflow}\left(1.0 + min(RT, 0.4)\right) \tag{3.71}$$

$$+\Delta H_{crossflow} = max(0.1066 - \Delta H_{crossflow}, 0) \tag{3.72}$$

$$f(+\Delta H_{crossflow}) = 6200(+\Delta H_{crossflow}) + 50000(+\Delta H_{crossflow})^2 \tag{3.73}$$

$$-\Delta H_{crossflow} = max(-(0.1066 - \Delta H_{crossflow}), 0) \tag{3.74}$$

$$f(-\Delta H_{crossflow}) = 75tanh\left(\frac{-\Delta H_{crossflow}}{0.0125}\right) \tag{3.75}$$

These correlations are implicit for the variable θ_t as it cannot be directly solved. Therefore, the Newton method was chosen again for this problem. Equation (3.70) is reformulated to define the Newton function:

$$f(\theta_t) = -35.088ln\left(\frac{h}{\theta_t}\right) + 319.51 + f(+\Delta H_{crossflow}) - f(-\Delta H_{crossflow}) - \frac{\rho(\frac{U}{0.82})}{\mu}\theta_t \tag{3.76}$$

The iterative process starts with an initial guest for θ_t and the new value is computed with:

$$\theta_t^{new} = \theta_t - \frac{f(\theta_t)}{f\prime(\theta_t)} \tag{3.77}$$

3.5 Roughness Amplification Model and Equations

The approach chosen to model the effect of the surface roughness is to implement the Roughness Amplification model from Dassler and al. [27]. This model adds one scalar transport equation to the system of equations:

$$\frac{\partial(\rho A_r)}{\partial t} + \frac{\partial(\rho u_j A_r)}{\partial x_j} - \frac{\partial}{\partial x_j}\left[\sigma_{ar}(\mu + \mu_t)\frac{\partial A_r}{\partial x_j}\right] = 0 \tag{3.78}$$

The conservative variable of this equation is the Amplification Factor A_r which is used to modify the production term of the $\tilde{Re}_{\theta_t}$ transport equation. Equation (3.24) is rewritten as follows:

$$P_{\theta_t} = \rho \frac{c_{\theta_t}}{t} \left[(1 - F_{\theta_t})(Re_{\theta_t} - \tilde{Re}_{\theta_t}) - F_{A_r} \right] \tag{3.79}$$

$$F_{A_r} = \begin{cases} c_{Ar2} A_r^3 & \text{if} \quad A_r < C_{A_r}, \\ c_{Ar3}(A_r - C_{A_r}) + c_{Ar2} C_{A_r}^3 & \text{if} \quad A_r \geq C_{A_r} \end{cases} \tag{3.80}$$

$$C_{A_r} = \sqrt{\frac{c_{Ar3}}{3 c_{Ar2}}} \tag{3.81}$$

with:

$$c_{Ar1} = 8.0 \quad c_{Ar2} = 0.0005 \quad c_{Ar3} = 2.0 \quad \sigma_{ar} = 10.0 \tag{3.82}$$

Notice Eq. (3.78) has no source terms. Instead, A_r is produced from the boundary condition. The increase of the local values of A_r causes a decrease of the local values of $\tilde{Re}_{\theta_t}$. As a result, the transition onset will happen with smaller flow disturbances [23]. The wall boundary condition for A_r is:

$$A_r|_{wall} = c_{Ar1} k^+ \tag{3.83}$$

The variable k^+ is an indication of the momentum loss and depends mainly on the wall shear stress τ_{wall} and the equivalent sand roughness height k_s with the following equation:

$$k^+ = \sqrt{\frac{\tau_{wall}}{\rho_{wall}}} \frac{k_s}{\nu} \tag{3.84}$$

3.5.1 $k - \omega$ Roughness Boundary Condition

The model was originally designed to be coupled with the $k\omega$-γ-$\tilde{Re}_{\theta t}$ model with modifications to the ω wall boundary condition to include the effect of the roughness. The following modified boundary condition from Langel [23] was first implemented:

$$\omega_{rough}|_{wall} = \frac{\mu_\tau^2 S_r}{\nu} \tag{3.85}$$

$$\mu_\tau = \sqrt{\frac{\tau_{wall}}{\rho_{wall}}} \tag{3.86}$$

and the variable S_r is computed with the following:

$$S_r = \begin{cases} \frac{50}{k^+}^2 & \text{if} \quad k^+ \leq 25, \\ \frac{100}{k^+} & \text{if} \quad k^+ > 25 \end{cases} \tag{3.87}$$

Later, a more accurate roughness boundary condition developed by Aupoix [33] using the Colebrook correlations were implemented. The reader is referred to the original references [33] for a complete description of the equations. Note that this boundary condition was selected to produce the results in Chapter 5.

3.5.2 SA Roughness Boundary Condition

To the best of our knowledge, the roughness amplification model has not been previously coupled with the SA-γ-$\tilde{Re}_{\theta t}$ model in the literature. However, as the SA turbulence model has demonstrated superior numerical performance and good results in Chapter 4, it is worth exploring the possibility of coupling the roughness model with the SA-γ-$\tilde{Re}_{\theta t}$ model in this study. It should be noted that the modified boundary condition of the $k-\omega$ model cannot be used as a replacement for the SA model. Instead, the strategy employed in this work is to use the modified boundary condition from the roughness extension proposed by Aupoix and Spalart [26].

The SA roughness boundary condition takes into account the effect of the roughness by increasing the turbulent eddy viscosity at the surface wall [26]. This causes an increase of the surface drag and wall heat flux level [26]. The first modification is to increase the wall distance d to take into account the roughness height k_s:

$$d_{new} = d + 0.03k_s \tag{3.88}$$

The definition of χ from Eq. (3.6) is changed:

$$\chi = \frac{\tilde{\nu}}{\nu} + c_{R1}\frac{k_s}{d_{new}} \tag{3.89}$$

with $c_{R1} = 0.5$. When the surface is smooth and $k_s = 0$, the definition returns to the original one. The last modification is the wall boundary condition which is changed to:

$$\frac{\partial\tilde{\nu}}{\partial n}|_{wall} = \frac{\tilde{\nu}_{wall}}{0.03k_s} \tag{3.90}$$

The roughness wall boundary condition of the variable μ_t needs to be changed to have the correct values when calculating the fluxes:

$$\mu_{t,wall} = \rho_{wall} f_{\nu 1,wall}\tilde{\nu}_{wall} \tag{3.91}$$

with:

$$f_{\nu 1,wall} = \lim_{d_{new}\to 0} \frac{\chi^3}{\chi^3 + C_{\nu 1}^3} = 1 \tag{3.92}$$

3.5.3 Leading Edge Roughness

Some experiments on airfoils like the ones conducted by Abbott and al. [34] have surface roughness from the leading edge to a percentage of the chord and smooth surface for the rest of the airfoil. In these instances, a simple modification is implemented to the boundary conditions of both models:

For the $k-\omega$ model:

$$\omega|_{wall} = \begin{cases} \omega_{rough} & \text{if} \quad x_{wall} \leq x_{rough}, \\ \omega_{smooth} & \text{else} \end{cases} \tag{3.93}$$

For the SA model:

$$\tilde{\nu}|_{wall} = \begin{cases} \tilde{\nu}_{rough} & \text{if} \quad x_{wall} \leq x_{rough}, \\ \tilde{\nu}_{smooth} & \text{else} \end{cases} \tag{3.94}$$

with x_{rough} the length of the region with roughness from the leading edge. Note that the roughness amplification equations remain unchanged.

3.6 CHAMPS Solver

These turbulence models are implemented in the unstructured multi-physic solver CHAMPS (CHapel Multi-Physics Simulation) [12]. This solver uses the finite volume method (FVM) discretization for the compressible RANS equations and the turbulence models. Refer to Appendix A for the steps of the FVM. Both systems of equations are solved in a segregated manner [31] and the jacobians are derived analytically. A second order Roe scheme is used for the convective fluxes of the RANS equations, while a first order upwing scheme is used for the turbulence models. Both systems of equations can be used in a pseudo-time accurate scheme using an explicit Runge-Kutta or an implicit backward-Euler algorithm in which the linear systems are solved with a Block SGS scheme or a GMRES solver [12]. An interesting feature is that CHAMPS is entirely written in the programming language Chapel. The interested reader can read on the Chapel attributes and its application to CHAMPS in [12].

CHAPTER 4 TRANSITION RESULTS

In this chapter, the SA-γ-$\tilde{Re}_{\theta t}$ and kω-γ-$\tilde{Re}_{\theta t}$ transition models are verified and validated. Section 4.1 presents a comparison between the two models to highlight their differences. It was found that the predicted transition locations using the SA-γ-$\tilde{Re}_{\theta t}$ model are too early for natural transition when compared to experimental data. As a result, in Section 4.2, the results of an investigation into this issue are presented, leading to the development of a correction which improves the prediction of natural transition. Finally, the results of the crossflow extension for 3D applications are presented in Section 4.3. Note that parts of this chapter are based on the reference of Bilodeau-Bérubé and al. [28].

4.1 Comparison of the SA-γ-$\tilde{Re}_{\theta t}$ and $k\omega$-γ-$\tilde{Re}_{\theta t}$ transition model

This section compares the SA-γ-$\tilde{Re}_{\theta t}$ and the $k\omega$-γ-$\tilde{Re}_{\theta t}$ transition models. The results of this study are produced for 2D cases. Grid refinement studies and transition locations as a function of the angle of attack are presented. The crossflow extension and roughness model are not used. The cases presented are the Schubauer and Klebanov flat plate case, and the NACA0012, S809 and NLF0416 airfoil cases to validate natural and separation-induced transition and the T3A flat plate case to validate bypass transition. The freestream conditions and type of transition are resumed in Table 4.1 for each case. Note that all simulations for the SA-γ-$\tilde{Re}_{\theta t}$ model use $\tilde{\nu}/\nu = 3$, as recommended by Spalart and Allmaras [13].

Table 4.1: Summary of freestream conditions for each case and type of transition (Natural (N), Separation-induced (S) and Bypass(B))

Case	Transition type	Re ($\times 10^6$)	Mach	$k\omega$-γ-$\tilde{Re}_{\theta t}$		SA-γ-$\tilde{Re}_{\theta t}$	
				μ_t/μ_l	Tu_∞ (%)	$\tilde{\nu}/\nu$	Tu_∞ (%)
S&K flat plate	N	5.00	0.20	1	0.10	3	0.03
NACA0012 airfoil	N + S	2.88	0.16	100	0.33	3	0.20
S809 airfoil	N + S	2.00	0.10	10	0.19	3	0.07
NLF0416 airfoil	N + S	4.00	0.10	10	0.15	3	0.15
T3A flat plate	B	1.00	0.20	12	2.20	3	1.80

4.1.1 S&K Flat Plate

The flat plate is a common geometry to validate the transition modelling. The experiment conducted by Schubauer and Klebanov (S&K) [5] in 1956 had a low freestream turbulence intensity of 0.03% and zero pressure gradient which are the ideal conditions to validate only the natural transition mechanism. The Mach number is 0.2 and the Reynolds number is 5×10^6. For the $k\omega$-γ-$\tilde{Re}_{\theta t}$ model, Tu_∞ was increased to 0.10% and $\mu_t/\mu_l = 1$ as recommended by Langtry [9]. Note that the values were not adjusted to increase the precision of the results with the experimental data, although it would be possible to conduct a better calibration in future work.

Grids and boundary conditions

The grids used for the simulations have rectangular shaped domain with farfield boundary condition at the inlet, outlet and top side and a symmetry boundary condition in front of the wall surface:

1. 545×193 grid points, generated with Pointwise
2. 545×385 grid points, from the NASA Turbulence Modelling Resource (TMR) [29]
3. 1089×385 grid points, generated with Pointwise

Note that the dimensions of the meshes are those proposed by the TMR [29].

Surface drag comparison

Figure 4.1 presents a comparison of the two models for various mesh sizes. The results are also compared to data from the S&K experiment [5]. The transition phenomenon can be observed in the rapid increase in skin friction from the laminar region. In the laminar region, both models match well with the experimental data. For the onset of transition, both models seem to converge to a similar value which is close to the experimental data. However, the length of the transition region after the onset is shorter than what is observed in the experimental data. This length is mainly influenced by the F_{length} correlation described in Section 3.3.4, and reducing its output could improve the results. However, this modification was not tested in this work. The turbulent skin friction curve after the transition is similar to the experimental data, but its height is slightly lower for both models. It is possible to recalibrate using the parameter β as discussed in Section 3.3.7. Finally, grid refinement tends to move the transition upstream for the SA-γ-$\tilde{Re}_{\theta t}$ model, so using a coarser grid may give

misleading results as it appears to be closer to the experimental data than the results of the refined meshes.

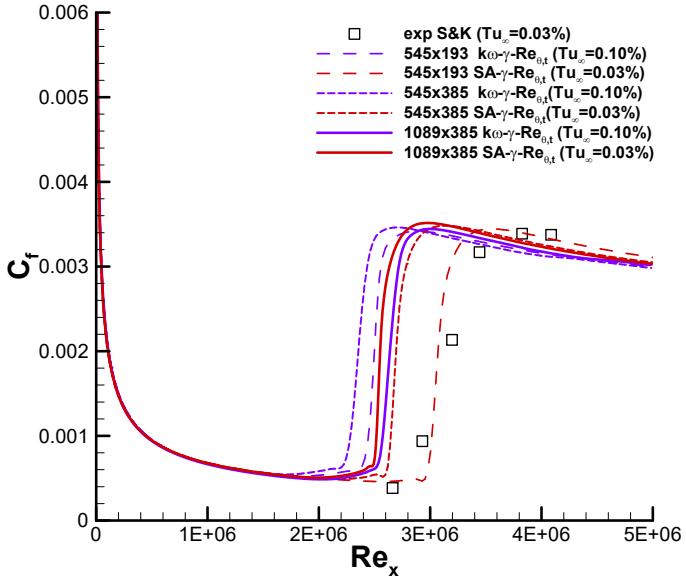

Figure 4.1 C_f in function of Re_x for the Schubauer and Klebanov flat plate case ($M = 0.2, Re = 5 \times 10^6$)

4.1.2 NLF0416 Airfoil

The NLF0416 airfoil was designed by Somers [4] with the goal of increasing natural-laminar flow (NLF) around the airfoil and reducing drag. This case is therefore interesting as the natural transition should be delayed compared to a common airfoil.

The results of this case are compared to the experimental data from the Low Turbulence Pressure Tunnel (LTPT) located at NASA Langley Research Center [4]. The Reynolds number of this data is 4.0×10^6 and the Mach number is 0.1. Since Tu_∞ was unknown for the experiment, the value of 0.15% is assumed for both models. It is consistent with the value chosen by Piotrowski and Zingg [21] and it is also the recommended value of the Transition Modelling and Predictive Capabilities Seminar (TCMPS) guidelines [35]. The transition mechanism is typically a natural transition for the upper side and a separation-induced transition for the lower side because of a very small laminar separation bubble that appears for $\alpha > 0°$.

Grid convergence study

A grid convergence study is performed on meshes of size 513×129, 1025×257 and 2049×513 and the results are shown on Figure 4.2. The convergence of C_D is acceptable, but there is a slight offset between the models which may be caused by the difference of the transition locations. There is no difference between the model for the pressure drag C_{Dp} (both curves are on top of each other) which means the difference in the total drag come from the friction drag only.

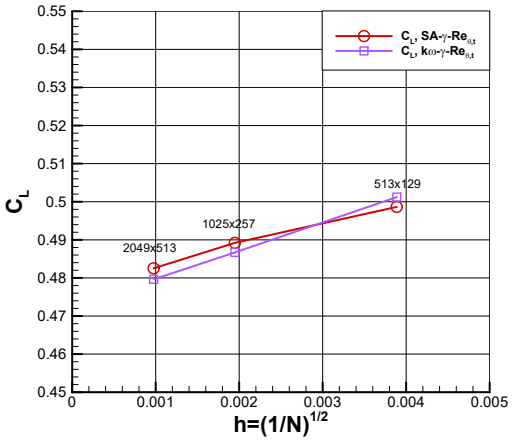

(a) C_L in function of the grid

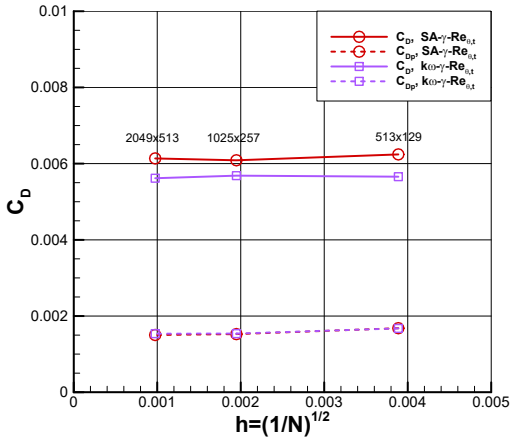

(b) C_D in function of the grid

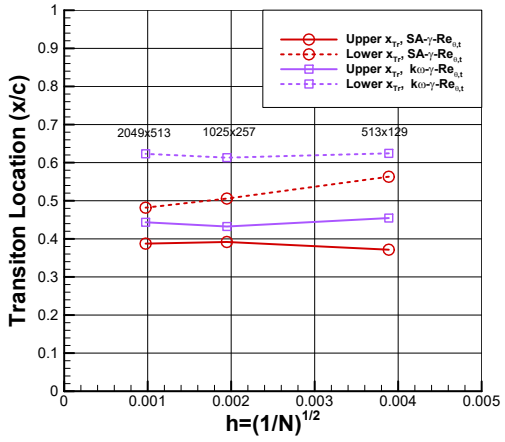

(c) X_{tr} in function of the grid

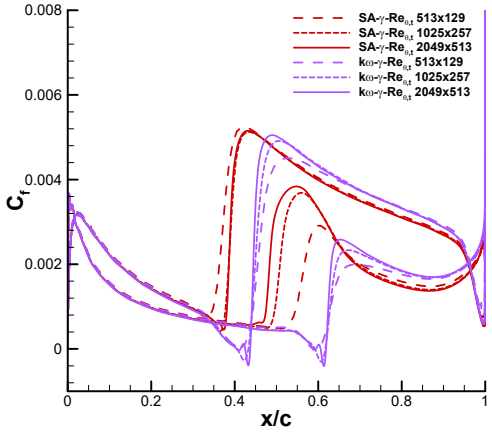

(d) C_f in function of the grid

Figure 4.2 Grid convergence study on NLF0416 case ($M = 0.10, Re = 4 \times 10^6, Tu_\infty = 0.15\%, AoA = 0.0°$)

For the transition location, the convergence is displayed on Figure 4.2c and the corresponding skin friction curves are shown on Figure 4.2d. The lower side of the SA-γ-$\tilde{R}e_{\theta t}$ model is more sensitive to grid refinement compared to the $k\omega$-γ-$\tilde{R}e_{\theta t}$ model. This can be explained by the natural transition mechanism of the SA-γ-$\tilde{R}e_{\theta t}$ model, which is more sensitive to grid resolution, compared to the separation-induced transition mechanism of the $k\omega$-γ-$\tilde{R}e_{\theta t}$ model.

Transition location study

Figure 4.3b displays a comparison of the lift coefficient as a function of the transition location. The experimental data is also shown. Note that each pair of experimental points corresponds to the beginning and the end of the transition region. The models are in good agreement with the experimental data in general, as most of the numerical points are close to or inside the experimental region. However, each model has one difficulty.

For the SA-γ-$\tilde{R}e_{\theta t}$ model, it predicts the natural transition to be too upstream on the lower side for $\alpha \leq 0^\circ$ ($C_L \approx 0.5$). Decreasing the turbulence intensity could delay the natural transition and improve the results on the lower side, but it would worsen the already good results on the upper side. This early natural transition is investigated in Section 4.2.

For the $k\omega$-γ-$\tilde{R}e_{\theta t}$ model, the results are too far downstream because the model does not capture the natural transition; instead, it is caused by a separation bubble downstream from the experimental data. Increasing Tu_∞ would increase the triggering of the natural transition, but this was not tested.

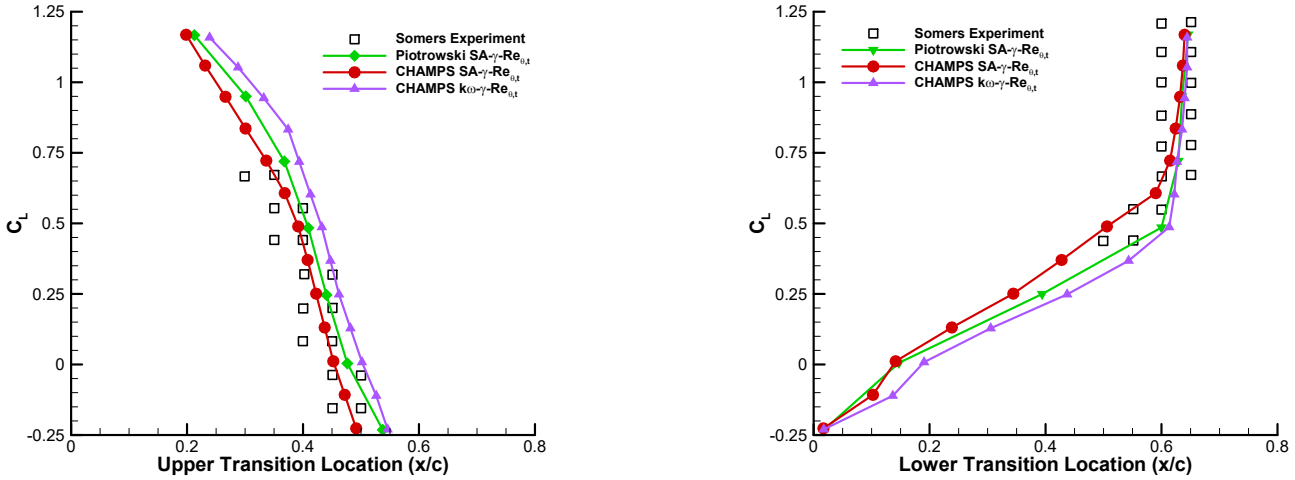

(a) NLF0416 upper surface

(b) NLF0416 lower surface

Figure 4.3 Transition locations in function of the angle of attack (AoA) for the NLF0416 case ($M = 0.10, Re = 4 \times 10^6, Tu_\infty = 0.15\%, grid = 1025 \times 257$)

4.1.3 F_{onset} parametric investigation

The parameters c_{opt1} and c_{opt4} can be modified to alter the behaviour of the F_{onset} equation (Equation 3.49), as discussed in Section 3.3.5. The S&K flat plate and NLF0416 airfoil cases were chosen for this investigation because the flat plate case has only a natural transition mechanism and the NLF0416 case has both natural and separation-induced transition mechanisms. Figure 4.4 shows the effect of the $\{c_{opt1}, c_{opt4}\}$ parameters on the transition location. The results are computed using the SA-γ-$\tilde{R}e_{\theta t}$ and $k\omega$-γ-$\tilde{R}e_{\theta t}$ models.

For the flat plate, Figure 4.4a shows that the transition onset is closer to the experimental values when the parameters are set to $\{1, 2\}$. Setting the parameters to $\{2, 2\}$ is most effective at moving the transition locations downstream, resulting in an overshoot of the experimental data. As previously discussed in Section 3.3.5, this is because there is no production of intermittency when the viscosity ratio is low with the parameters set to $\{2, 2\}$.

When the parameters are set to $\{2, 4\}$, Figure 3.3d shows that it increases the F_{onset1} transition criteria of Equation (3.46) from 1.0 to approximately 1.2, which triggers the growth of intermittency. This pushes the transition downstream, as observed in Figure 4.4a. It can

also be seen that the $k\omega$-γ-$\tilde{R}e_{\theta t}$ model is more affected by this change, although the reason is unknown.

On the other hand, when the parameters are set to $\{1, 4\}$, it increases the maximum value of F_{onset}, but it has a minimal impact on the transition locations for both models. One possible reason for this, as seen in Figure 3.3, is that F_{onset} on Figure 4.4a did not reach its maximum value and may have stayed in the region where $F_{onset1} < 1.2$.

For the NLF0416 case, when the parameters are set to $\{2, 2\}$ or $\{2, 4\}$, Figure 4.4b shows that the transition locations are pushed downstream on both surfaces, but the process appears to be halted by the laminar separation bubbles. As shown in Figure 4.3, the original values of $\{1, 2\}$ for the parameters are more desirable because the results of the SA-γ-$\tilde{R}e_{\theta t}$ and $k\omega$-γ-$\tilde{R}e_{\theta t}$ models are already somewhat downstream of the experimental data.

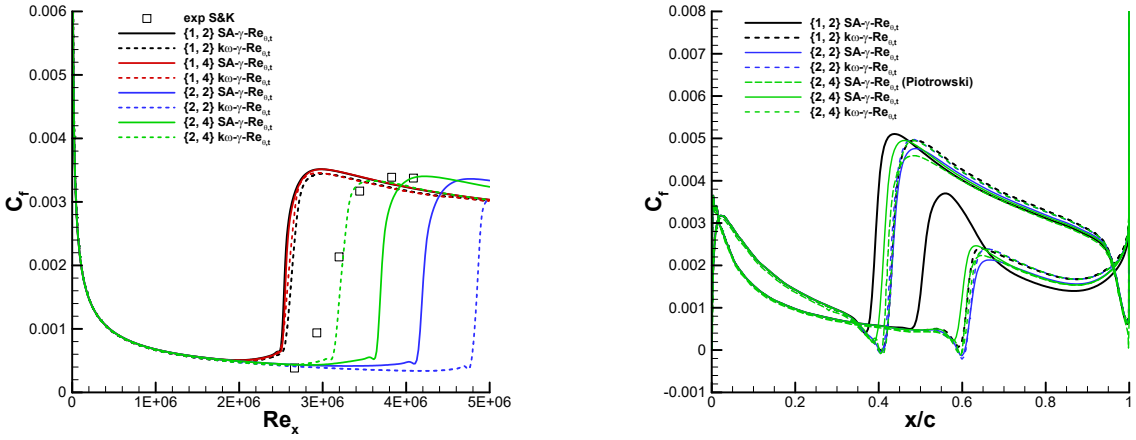

(a) C_f in function of Re_x for the S&K flat plate ($grid = 1089 \times 385, M = 0.20, Re = 5 \times 10^6$)

(b) C_f in function of x/c for the NLF0416 airfoil ($grid = 1025 \times 257, M = 0.10, Re = 4 \times 10^6, Tu_\infty = 0.15\%, AoA = 0.0°$)

Figure 4.4 Effect of the F_{onset} parameters $\{c_{opt1}, c_{opt4}\}$ on the transition for the S&K and NLF0416 cases

4.1.4 NACA0012 Airfoil

The NACA0012 is a symmetric airfoil developed at the Langley Research Center. The experimental data is from Gregory and O'Reilly in a study conducted in a wind tunnel in 1973 [6]. The Reynolds number is 2.88×10^6 and the Mach number is 0.16. The turbulence intensity of the experiment is unknown, therefore the value of 0.20% is selected for the SA-γ-$\tilde{Re}_{\theta t}$ which is the same value used in the work of Piotrowski and Zingg [21]. For the $k\omega$-γ-$\tilde{Re}_{\theta t}$ model, the freestream values are 0.33% for Tu_∞ and 100 for μ_t/μ_l which is consistent with the values used in the work of Barouillet and al. [30]. This case has a natural transition mechanism for $\alpha < 8°$ and separation induced transition mechanism when testing at higher angles of attack [6].

Grid convergence study

A grid convergence study at $\alpha = 0°$ is performed on meshes of size 513×129, 1025×257 and 2049×513 and the results are shown in Figure 4.5. It displays the convergence of the drag coefficient and the transition location. The lift is not presented since the airfoil is symmetric and produces 0.0 lift for all meshes to within 1×10^{-7}. Both convergences are acceptable since the sensitivity to the grid refinement is low. The pressure drag C_{Dp} is fully converged for all grids and the models match. The small offset between the models seen with the drag is explained by the difference in the transition locations.

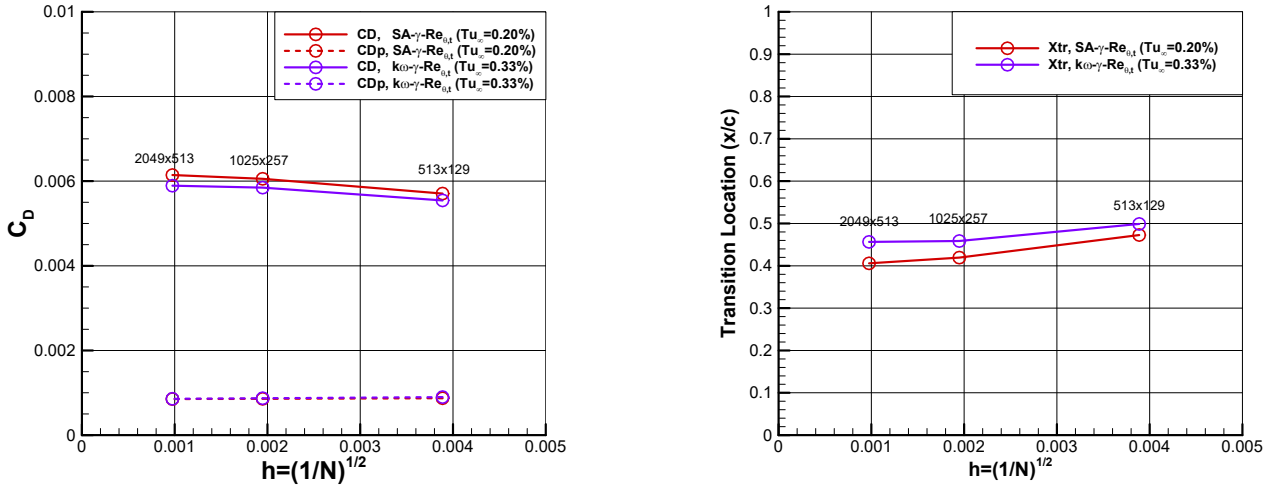

(a) C_D in function of the grid

(b) X_{tr} in function of the grid

Figure 4.5 Grid convergence study on the NACA0012 airfoil case ($M = 0.16, Re = 2.88 \times 10^6, AoA = 0.0°$)

Transition location study

Computational results of the transition locations of both models are displayed and compared to the experimental data on Figure 4.6. The numerical results from Piotrowski and Zingg [21] using the SA-γ-$\tilde{Re}_{\theta t}$ model is also shown for comparison purposes.

On the lower side, the SA-γ-$\tilde{Re}_{\theta t}$ model is more inline with the experimental data overall and the results are also very similar to the results of Piotrowski and Zingg [21]. However, the $k\omega$-γ-$\tilde{Re}_{\theta t}$ model matches at $\alpha = 0°$. This is due to the slope of the curve of the $k\omega$-γ-$\tilde{Re}_{\theta t}$ model which is less consistent with the experimental data compared to the SA-γ-$\tilde{Re}_{\theta t}$ model. There is also an indication of early natural transition with the SA-γ-$\tilde{Re}_{\theta t}$ model since the results are slightly too early, as seen with the other cases.

For the upper side, the transition location seems too far upstream compared to the experimental data. This is mainly due to the transition criteria of Eq. (3.32) which estimates the location approximately in the middle of the very long transition region of these points. But the actual transition onset is closer to the experimental data. In contrast, the transition locations match well with the experimental data for $\alpha \geq 8°$ as the transition mechanism switches to separation-induced.

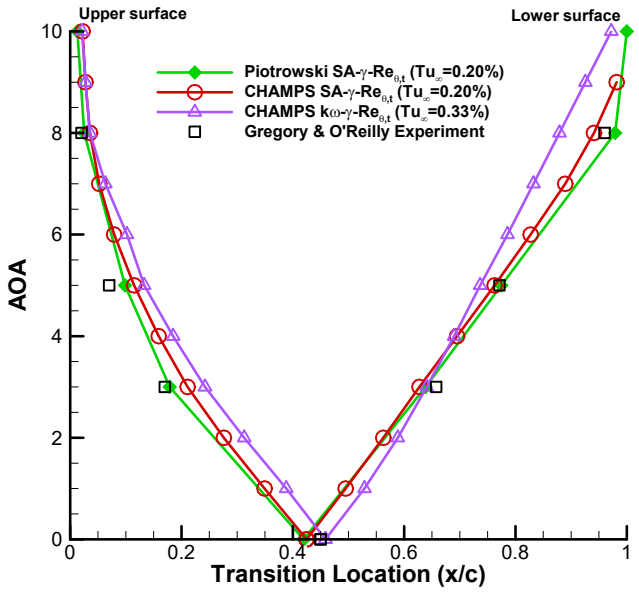

Figure 4.6 Transition locations in function of the angle of attack for the NACA0012 airfoil case ($grid = 1025 \times 257, M = 0.16, Re = 2.88 \times 10^6$)

4.1.5 S809 Airfoil

The S809 is a wind-turbine airfoil designed by Somers [3] with the objective of restraining the maximum lift, reducing the sensitivity to surface roughness and having a low-profile drag. This airfoil is thicker than a conventional airplane airfoil and the shape allows laminar separation bubbles to appear on both sides for the angle of attack up to approximately 5°. For angles of attack superior to 5°, the upper transition switches to a natural transition mechanism and the transition location moves quickly near the leading edge.

The experimental results were obtained in the wind tunnel of the Delft University of Technology Low-Speed Laboratory [3]. The data showed in this paper is for a Reynolds number of 2.0×10^6 and a Mach number of 0.10. The transition location was measured with microphones and the experimental turbulence intensity is varying from 0.02% to 0.04%.

Computational results were produced with a mesh of size 1025×257. A sensitivity study of the influence of the turbulence intensity was conducted at an angle of attack of 6° where the transition mechanism is a natural transition. The results are displayed on Figure 4.7 for the SA-γ-$\tilde{Re}_{\theta t}$ model. It shows that the turbulence intensity has almost no influence on the lower side of the airfoil where the transition regime is a separation-induced mechanism. For the rest of the study, a freestream turbulence intensity of 0.07% is selected for the SA-γ-$\tilde{Re}_{\theta t}$ model as recommended by the TCMPS guidelines [35]. In the case of the $k\omega$-γ-$\tilde{Re}_{\theta t}$ model, the values selected in the freestream are 0.19% for the turbulence intensity and $\mu_t/\mu_l = 10$ in order to have the natural transition consistent with the experimental data.

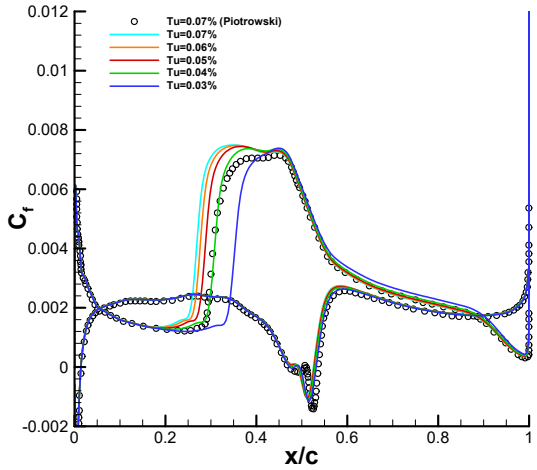

Figure 4.7 Sensitivity study of the C_f along x/c with varying turbulence intensity on the S809 airfoil case using SA-γ-$\tilde{Re}_{\theta t}$ ($M = 0.10, Re = 2 \times 10^6, grid = 1025 \times 257$)

Grid convergence study

A grid convergence study was conducted using meshes of size 513×129, 1025×257 and 2049×513 at an angle of attack of $6°$. The results are presented in Figure 4.8 and shows similar behaviour to other airfoil cases. The convergence of the transition location on Figure 4.8c is achieved quicker for the lower side than the upper side. This is because the lower side transition regime is separation-induced and natural transition is more sensitive to the grid resolution.

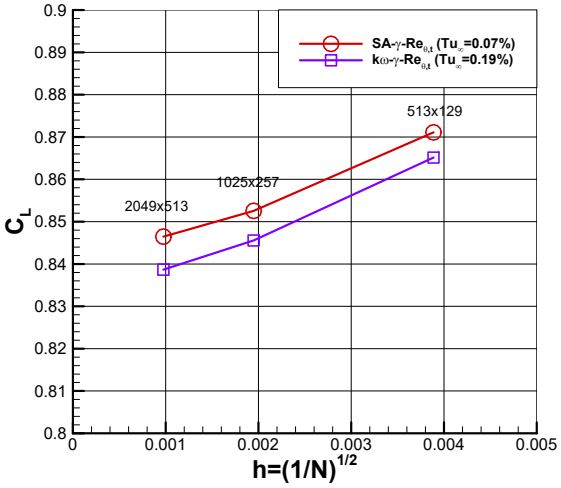

(a) C_L in function of the grid

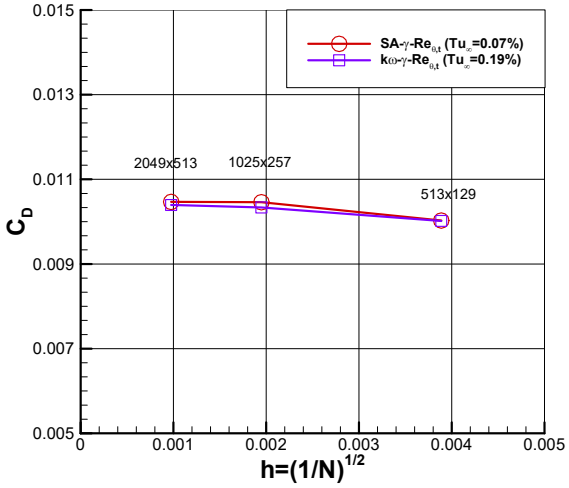

(b) C_D in function of the grid

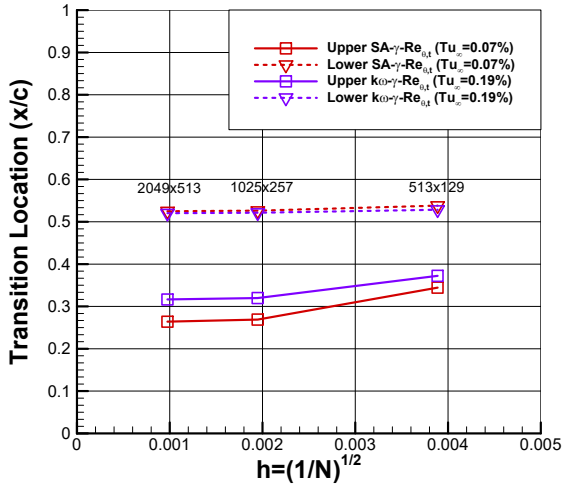

(c) X_{tr} in function of the grid

Figure 4.8 Grid convergence study on the S809 airfoil case ($M = 0.10, Re = 2 \times 10^6, \alpha = 6.0°$)

Natural transition sensitivity to grid refinement

There is a possible explanation from the work of Nie [36] in which he discussed the sensitivity of the natural transition location being dependent on the growth of the vorticity Reynolds number Re_ν which itself is very sensitive to the normal-wall grid resolution. Furthermore, the separation-induced transition mechanism depends on strong adverse pressure gradients as discussed in [9]. Therefore, this could explain why the separation-induced transition is more independent of the grid resolution and more affected by the profile's geometry and the flow conditions.

Transition location study

Figure 4.9 displays the upper and lower transition locations varying with the angle of attack of the S809 airfoil case. For the upper side, the prediction is better at $\alpha \leq 5°$ where the transition mechanism is separation-induced transition. For the lower side, the transition mechanism is only separation-induced and the results are in very good agreement with the experimental data for all angles of attack. This supports that the model is better at predicting this type of transition.

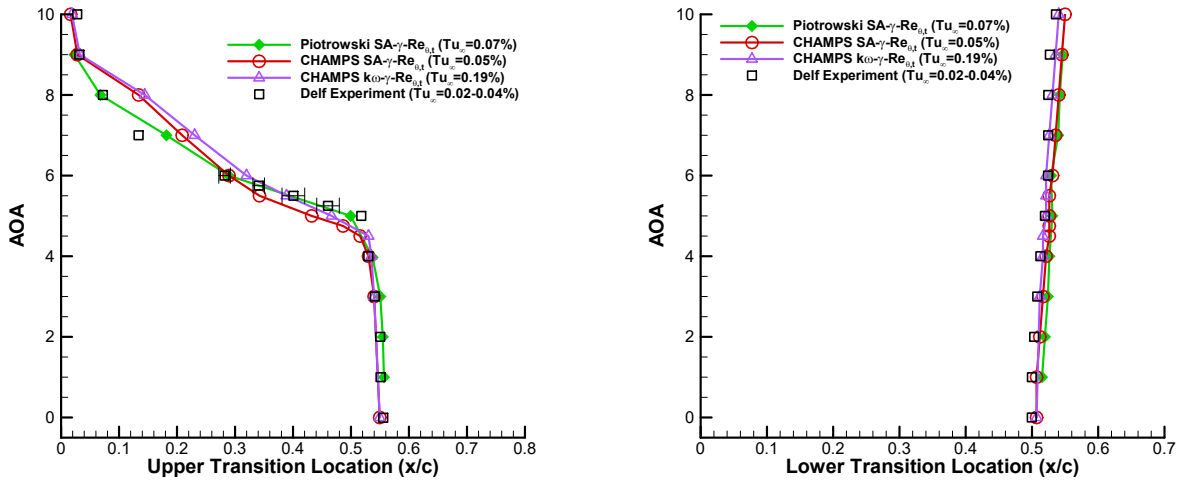

(a) S809 upper surface

(b) S809 lower surface

Figure 4.9 Transition locations in function of the angle of attack on the S809 airfoil case ($grid = 1025 \times 257, M = 0.10, Re = 2 \times 10^6$)

4.1.6 T3A Flat Plate

The last test case for this section is the T3A flat plate from the ERCOFTAC (European Research Community on Flow, Turbulence and Combustion) commonly used to validate the transition in the bypass regime due to the higher level of turbulence intensity. The experiment was conducted by Savill in the early 1990s [37]. For the flow condition, the Reynolds number is 1.0×10^6 and the Mach number is 0.2. The turbulence intensity is 3.3% at the inlet of the flat plate, but the decay of the turbulence must be taken into account since it has a strong effect on this case.

In the proposed method, the control decay correction of the $k\omega$-γ-$\tilde{R}e_{\theta t}$ model is used to prevent the decrease of Tu. The value of Tu_∞ is then selected to correspond to the experimental Tu near transition. According to [13], the decay causes Tu to be approximately 1.9% near the experimental transition location. Therefore, different values for Tu_∞ were tested, and 1.8% was selected for the SA-γ-$\tilde{R}e_{\theta t}$ model and 2.2% for the $k\omega$-γ-$\tilde{R}e_{\theta t}$ model.

Figure 4.10 presents the result of the skin friction drag which is compared to the experimental data along with the laminar Blasius coefficient for reference. The grid used has a size of 1089×385 and has the same topology of the S&K flat plate case in Section 4.1.1. The onset of the transition correlates well to the experimental data. However the length of the transition is shorter for the SA-γ-$\tilde{R}e_{\theta t}$ model which is consistent with what was observed with the S&K flat plate case. Moreover, the $k\omega$-γ-$\tilde{R}e_{\theta t}$ model is also more inline with the experimental data in the region before the transition. This suggests that the $k\omega$-γ-$\tilde{R}e_{\theta t}$ model starts to trigger the transition process earlier while the SA-γ-$\tilde{R}e_{\theta t}$ model follows the laminar curve longer, but the transition length is shorter when it occurs.

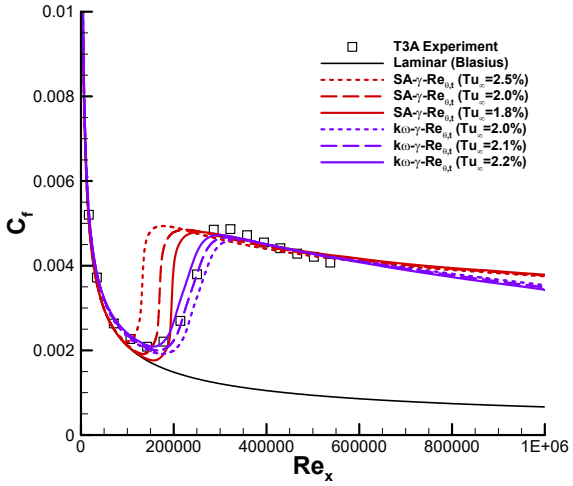

Figure 4.10 C_f in function of x/c for the T3A flat plate case ($grid = 1089 \times 385, M = 0.2, Re = 1 \times 10^6$)

4.2 Investigation of Early Natural Transition

The results from Section 4.1 showed that the prediction of the transition location is accurate when the type of transition is separation-induced. But when the transition type is natural, there is often an offset between the SA-γ-$\tilde{R}e_{\theta t}$ model and the experimental data. The trend is that the simulated transition locations are too far upstream. For this reason, an investigation was carried out to find out the possible cause of the early natural transition.

This study was mostly conducted on the S&K flat plate, the NACA0012 and NLF0416 airfoil cases. However, the S&K flat plate case was chosen for the analysis since it is a natural transition only case. The F_{onset} equation 3.49 of the transition model is examined with this case. As discussed in Section 3.3.5, this equation depends on two variables whose influence can trigger the transition:

1. The viscosity ratio RT
2. The transition criteria F_{onset1}

Analysis

Figure 4.11a displays the solution of F_{onset1} and RT in the field above the flat plate. The experimental and numerical transition onset lines are also showed to highlight the early natural transition along three streamlines that pass in the transition region. The evolution of F_{onset1} and RT along these streamlines is plotted in Figure 4.11b and compared to the plot of the F_{onset} function. The transition process should behave according to the following rules:

1. The transition process should begin when $F_{onset1} > 1.0$ and be fully triggered when $F_{onset1} \geq 1.2$
2. The process should be maintained by the increase of the viscosity ratio RT [9]

However, streamlines 1 and 2 experience an increase in RT before the transition criterion $F_{onset1} > 1$ is met, causing an increase in F_{onset}. This indicates that RT is improperly triggering the transition before F_{onset1}. Another important observation from Figure 4.11a is that the location where $F_{onset1} \geq 1.2$ approximately matches the experimental transition onset. Therefore, the numerical transition location would be closer to the experimental data without RT triggering the transition.

Proposed solution

The proposed solution is to reduce the influence of RT on the triggering of the transition in the laminar region. This is achieved by calibrating a new parameter named C_{fo3} whose original value is 2.5 in Eq. (3.48). The equation is rewritten as:

$$F_{onset3} = max(1 - \frac{RT^3}{C_{fo3}^3}, 0) \tag{4.1}$$

C_{fo3} is the value of RT at which F_{onset} starts to increase on the RT axis. Figure 4.12 shows the effect of increasing the value of C_{fo3} on the F_{onset} function. It can be observed that an increase in value of 4.5 reduces the early influence of RT along the streamline 1 before it reaches the transition criteria $F_{onset1} > 1$.

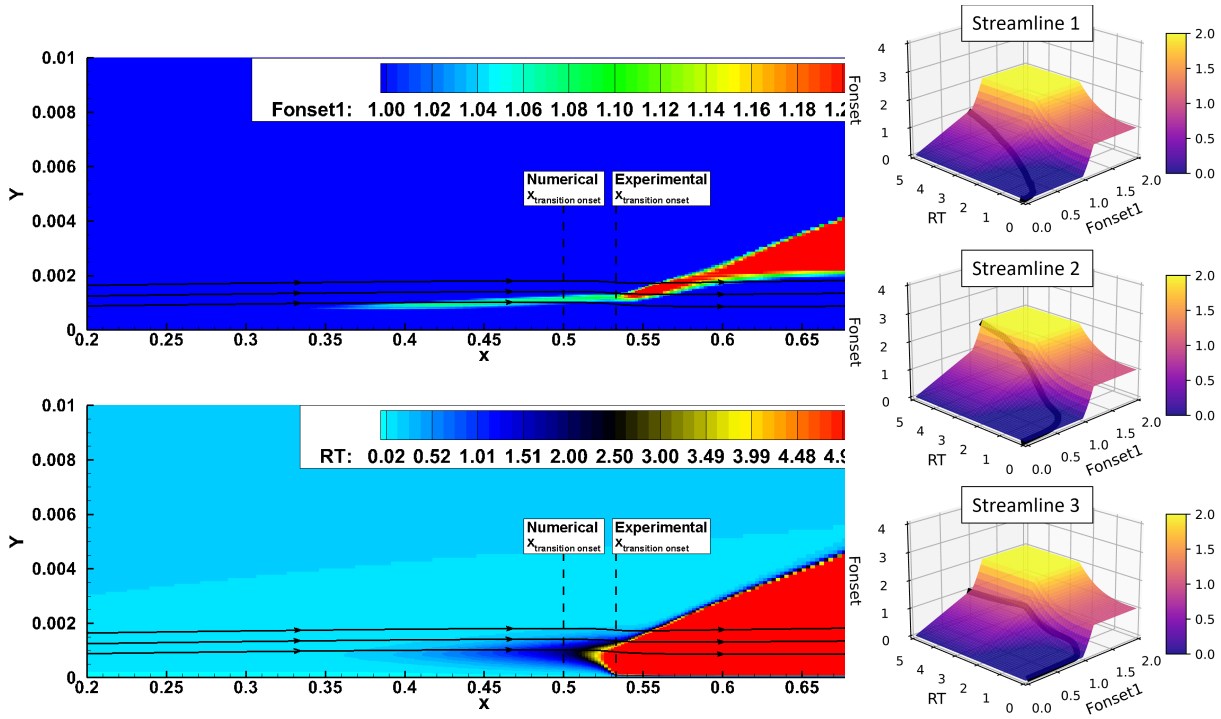

(a) Solution of F_{onset1} and RT in the field

(b) Corresponding streamlines along F_{onset}

Figure 4.11 Investigation of early natural transition on the S&K flat plate case ($M = 0.2, Re = 5 \times 10^6, grid = 1089 \times 385$)

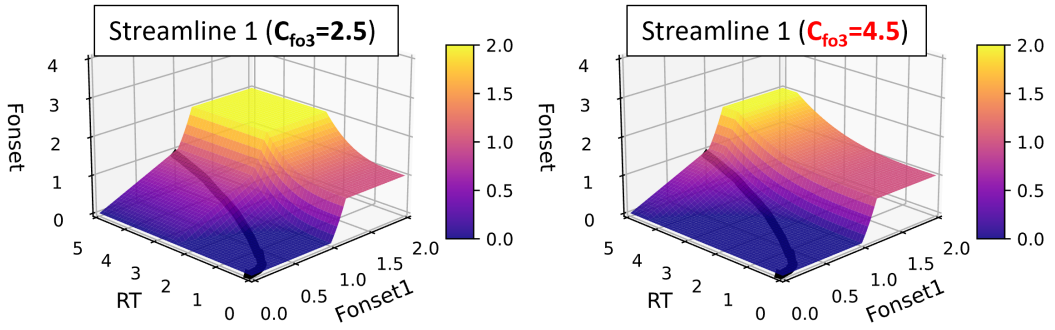

Figure 4.12 Effect of C_{fo3} on the F_{onset} function along the streamline 1 from Figure 4.11b

Results with the correction

Different values of C_{fo3} were tested up to 10. It was found that values greater than 5.0 could cause the natural transition mechanisms to stall, as expected. This happens when F_{onset1} reduces too quickly and RT cannot start maintaining the process. The value of $4.5 - 5$ was found to improve the results for most of the cases.

The results with the correction are displayed for the S809 airfoil case in Figure 4.13, for the NLF0416 airfoil case in Figure 4.14, for the S&K flat plate case in Figure 4.15, and for the NACA0012 airfoil case in Figure 4.16. These results show that the natural transition locations are more inline with the experimental data. Most importantly, the separation-induced transition locations that were in agreement with the experimental data are barely affected. However, in a few cases where the natural transition was already too far downstream, such as the upper side of the S809 and NACA0012 airfoils, this calibration pushes the transition even further downstream. However, since the correction tends to increase the length of the transition, this is partly due to the transition criteria (3.32) which calculates the location roughly in the middle of the transition region.

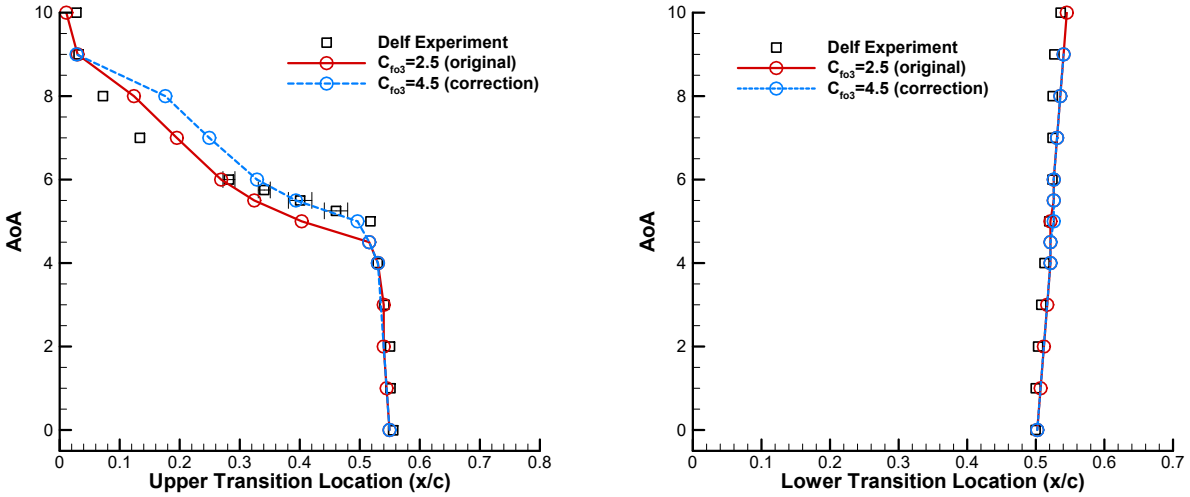

(a) Upper airfoil surface

(b) Lower airfoil surface

Figure 4.13 Transition location in function of AoA on S809 airfoil and effect of Cfo3 correction. Experimental data is from Somers [3]. ($M = 0.10, Re = 2 \times 10^6, Tu_\infty = 0.07\%, grid = 1025 \times 257$)

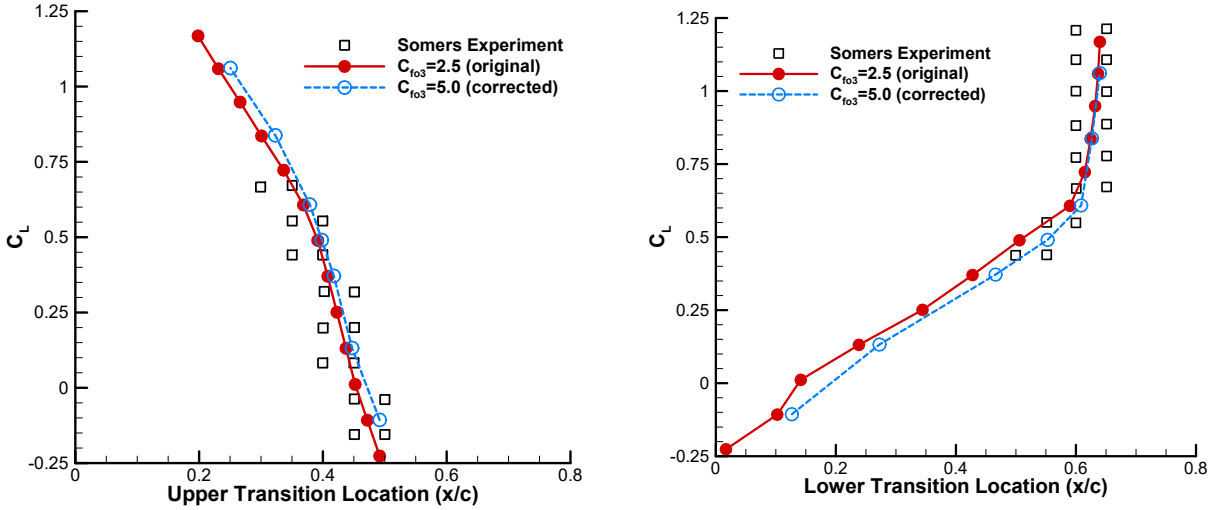

(a) Upper airfoil surface

(b) Lower airfoil surface

Figure 4.14 Transition location in function of the lift on NLF0416 airfoil and effect of Cfo3 correction. Experimental data is from Somers [4]. ($M = 0.10, Re = 4 \times 10^6, Tu_\infty = 0.15\%, grid = 1025 \times 257$)

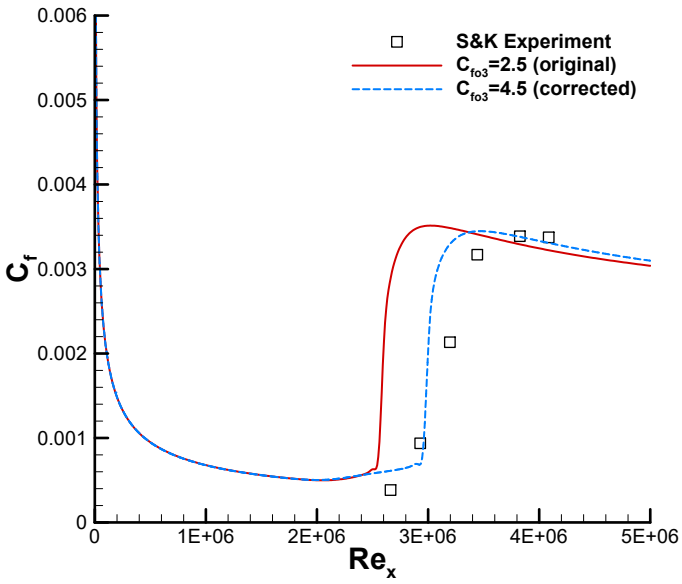

Figure 4.15 Comparison of C_f in function of Re_x for the Schubauer and Klebanov [5] flat plate case ($M = 0.2, Re = 5 \times 10^6, grid = 1089 \times 385$)

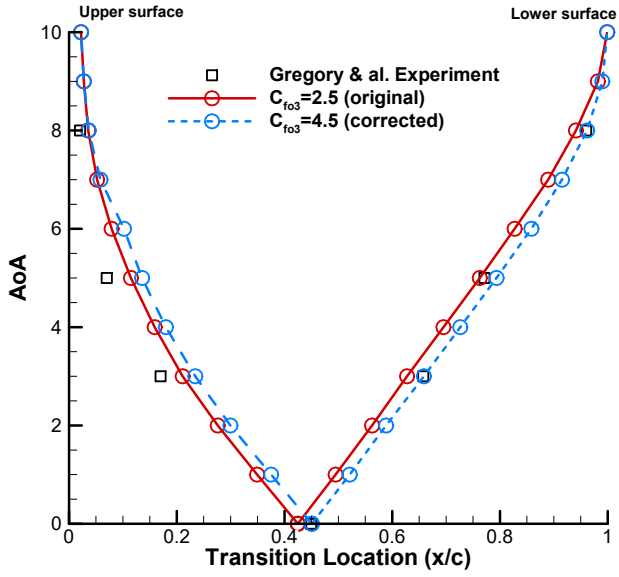

Figure 4.16 Transition location in function of AoA for the NACA0012 airfoil. Experimental data is from Gregory and O'Reilly [6] ($M = 0.16, Re = 2.88 \times 10^6, Tu_\infty = 0.20\%, grid = 1025 \times 257$)

4.3 Crossflow Results for 3D Cases

4.3.1 Inclined Prolate Spheroid

This case was used to validate the crossflow model in the work of Langtry and al. [32]. It is also a common test case of the AIAA transition modelling workshop. The conditions are an angle of attack of 15° with a Reynolds number of 6.5×10^6 and a Mach number of 0.13. The turbulence intensity is 0.10% which normally allows natural transition. However, since the angle of attack is high and the geometry has strong 3D curvature, the transition is mainly caused by the crossflow instabilities.

Figure 4.17 presents the friction drag for the SA-γ-$\tilde{Re}_{\theta t}$ and $k\omega$-γ-$\tilde{Re}_{\theta t}$ models using a grid of size 96×11250. The transition line of the experimental data is shown for comparison. The crossflow transition is well predicted overall with very small differences with the experimental transition line. It is slightly delayed for the $k\omega$-γ-$\tilde{Re}_{\theta t}$ model compared to the SA-γ-$\tilde{Re}_{\theta t}$ model.

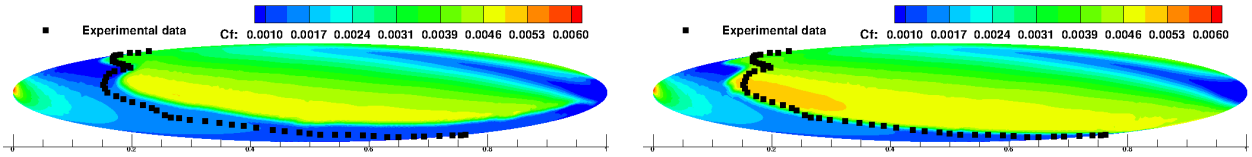

(a) $k\omega$-γ-$\tilde{Re}_{\theta t}$ model (b) SA-γ-$\tilde{Re}_{\theta t}$ model

Figure 4.17 Skin friction drag of the Prolate Spheroid case ($k_s = 3.3 \times 10^{-6}, M = 0.13, Re = 6.5 \times 10^6, AoA = 15°, Tu_\infty = 0.10\%, grid = 96 \times 11250$)

4.3.2 Sickle wing

The TU Braunschweig sickle wing was specifically designed to increase the crossflow instabilities, hence becoming a relevant, if not required, case for validating transition models with crossflow extension. The wing has three span-wise sections with increasing sweep angle corresponding to 30, 45 and 55 degrees which amplify the crossflow. Petzold and Radespiel [38] conducted an experiment with a Reynolds number of 2.75×10^6, a Mach number of 0.16 and a freestream turbulence intensity of 0.17%. A similar experiment was also conducted in a larger wing tunnel in the work of Kruze and al. [1]. The turbulence intensity was 0.053%, the Mach number was 0.175 and different Reynolds number and angle of attacks were tested

representing case A, B, C and D [1]. The flow conditions of each case are presented in Table 4.2.

Table 4.2: Different flow conditions of the sickle wing case [1]

	Re	α
Case A	2.75×10^6	$-2.6°$
Case B	4.5×10^6	$-2.6°$
Case C	4.5×10^6	$-0.3°$
Case D	2.75×10^6	$6.0°$

Note that the results and analysis presented in this section focus on Case A only in order to not overload the document. Some results with Case B and C are shown in Appendix C.

Meshes

The geometry was generously provided by the DLR and used to generate two types of unstructured mesh shapes and topologies using the software *Pointwise*. The first type of mesh has a hemisphere-shaped domain bounded by a farfied boundary condition. Three meshes of this kind were created with different refinement level and grid distribution and are referred as Mesh 1, 2 and 3 in Table 4.3. The second type of mesh topology is referred to as Mesh 4 and has the domain shape of the wind tunnel of the experiment [1]. The mesh is more refined near the three section borders, and the wing is at a $-2.6°$ angle to the tunnel to simulate Case A and B. The topology of Mesh 3 and 4 are respectively displayed on Figure 4.18 and 4.19. The description of all meshes is resumed in Table 4.3.

Table 4.3: Description of the different meshes used for the sickle wing case

Mesh #	Domain Shape	Grid Level	Total Cell Count	$\Delta s_0/c$ (initial step)
1	Hemisphere	Medium	8.10×10^6	2.50×10^{-6}
2	Hemisphere	Fine	12.5×10^6	2.50×10^{-6}
3	Hemisphere	Extra Fine	20.3×10^6	2.50×10^{-6}
4	Wind tunnel	Extra Fine	20.7×10^6	2.50×10^{-6}

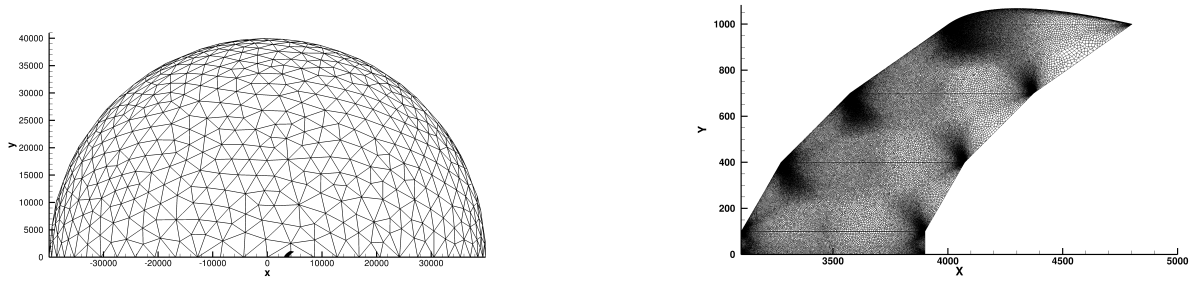

(a) Outside view (b) Upper surface view

Figure 4.18 Sickle wing Mesh 3 topology (see Table 4.3 for description)

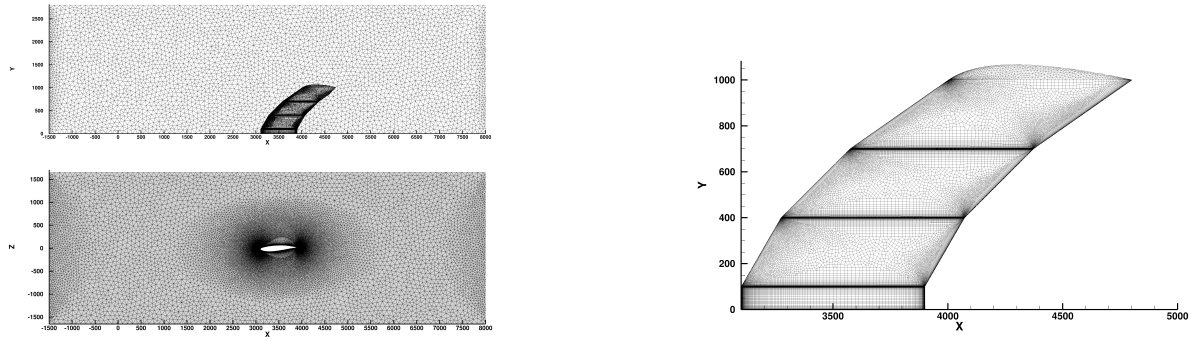

(a) Outside view (b) Upper surface view

Figure 4.19 Sickle wing Mesh 4 topology (see Table 4.3 for description)

Models comparison

To compare the effect of each model on the crossflow-induced transition, Mesh 4 was selected for this study since it has the highest resolution and is more representative of the wind tunnel experiment. The skin friction coefficient using the $k\omega$-γ-$\tilde{Re}_{\theta t}$ and SA-γ-$\tilde{Re}_{\theta t}$ models are compared in Figure 4.20 along with the Case A experimental transition line from Kruze [1]. The predicted transition line can be noticed by the sharp increase in skin friction. Both models can predict crossflow-induced transition. However, the $k\omega$-γ-$\tilde{Re}_{\theta t}$ model is more accurate at predicting the particular shape of the transition.

For the SA-γ-$\tilde{Re}_{\theta t}$ model, the spike-shaped transition line at the border sections seems accurate, like with the $k\omega$-γ-$\tilde{Re}_{\theta t}$ model, but the transition occurs too early overall. On the lower side, the transition mechanism is natural and is accurately predicted with the $k\omega$-γ-$\tilde{Re}_{\theta t}$ model, but the activation of crossflow seems to be too sensitive for the SA-γ-$\tilde{Re}_{\theta t}$ model as the transition occurs too early, once more.

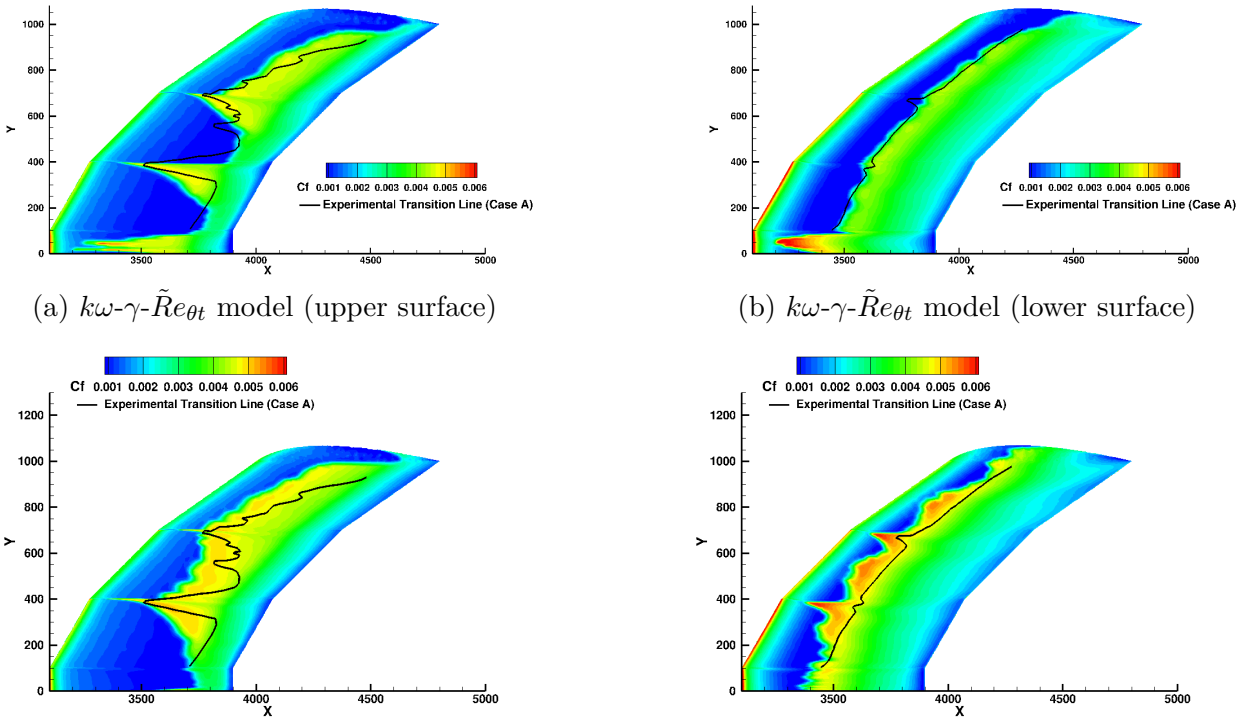

(a) $k\omega$-γ-$\tilde{R}e_{\theta t}$ model (upper surface)

(b) $k\omega$-γ-$\tilde{R}e_{\theta t}$ model (lower surface)

(c) SA-γ-$\tilde{R}e_{\theta t}$ model (upper surface)

(d) SA-γ-$\tilde{R}e_{\theta t}$ model (lower surface)

Figure 4.20 Sickle Wing Case A models comparison of skin friction using Mesh 4 overlaid with experimental transition lines from Kruze & al. [1] ($Re = 2.75 \times 10^6, \alpha = -2.6°$)

Effect of the grid refinement

To investigate the impact of different mesh resolutions, a comparison of skin friction using Mesh 1, 2, and 3 is presented in Figure 4.21 for Case A, and using the SA-γ-$\tilde{R}e_{\theta t}$ model only. The meshes have 8.1 million, 12.5 million, and 20.3 million cells, respectively, as described in Table 4.3. The general shape of the transition seems accurate, although the transition occurs somewhat too early, as seen with Mesh 4. For the lower side, the transition is more inline with the experimental data for all meshes compared to the previous results using Mesh 4, shown in Figure 4.20d. This means that crossflow-induced transition is very sensitive to the mesh topology. Moreover, increasing the resolution has less of an effect than expected, but it has improved the accuracy of the transition to some degree. In fact, the shape of the first spike from the root is sharper, and the transition line near the tip of the wing is pushed closer to the experimental line. On the lower side, the transition line is slightly improved, but the intensity of the two small spikes remains over-predicted.

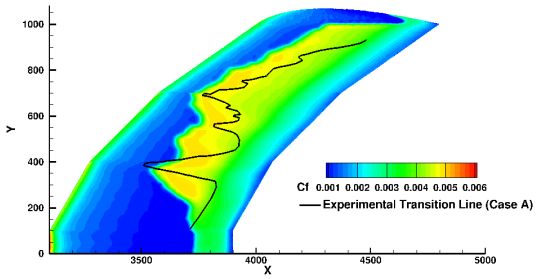

(a) Mesh 1 upper surface (8.10M cells)

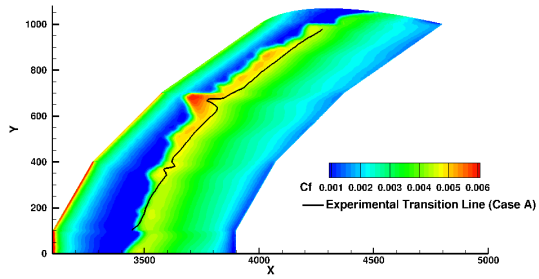

(b) Mesh 1 lower surface (8.10M cells)

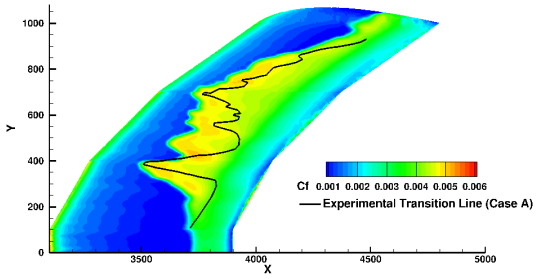

(c) Mesh 2 upper surface (12.5M cells)

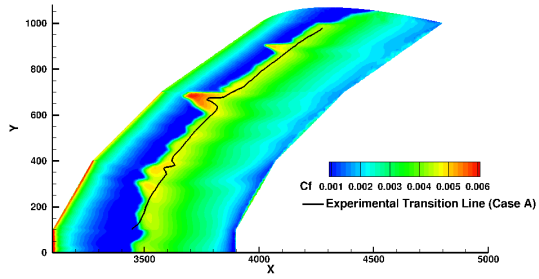

(d) Mesh 2 lower surface (12.5M cells)

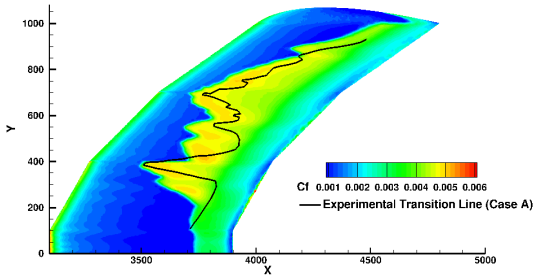

(e) Mesh 3 upper surface (20.3M cells)

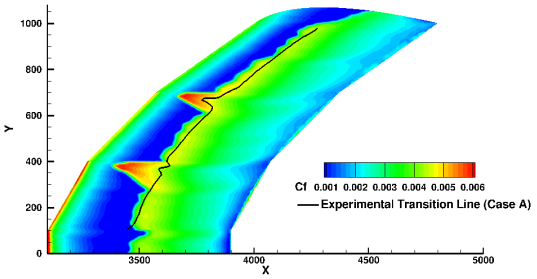

(f) Mesh 3 lower surface (20.3M cells)

Figure 4.21 Sickle Wing Case A Effect of grid refinement on skin friction using the SA-γ-$\tilde{R}e_{\theta t}$ model overlaid with experimental transition lines [1] ($Re = 2.75 \times 10^6, \alpha = -2.6°$)

Effect of mesh topology

To further study the effect of mesh topology, a comparison of skin friction using Meshes 3 and 4 is presented in Figure 4.22, for Case A and using the $k\omega$-γ-$\tilde{R}e_{\theta t}$ model. The two meshes are extra-fine grids with a very similar number of cells, so the difference comes only from the shape of the domain and topology. Note that the density residual of both simulations converged by at least 8 orders of magnitude.

In Figure 4.22, the simulation with Mesh 3 fails to predict the first spike compared to the one with Mesh 4, although the second spike is well predicted for Mesh 3. It is likely that the increased refinement of Mesh 4 near the section borders is what is causing the difference, but it is also possible that the difference originates from the domain shape of Mesh 4, which has the shape of the wing tunnel from the experiment. For the lower surface, there is almost no difference between the two simulations, except for Mesh 3, which is slightly more accurate at predicting the small spike closer to the root. Nevertheless, it is clear that crossflow-induced transition is very sensitive to the mesh compared to the natural transition seen on the lower surface.

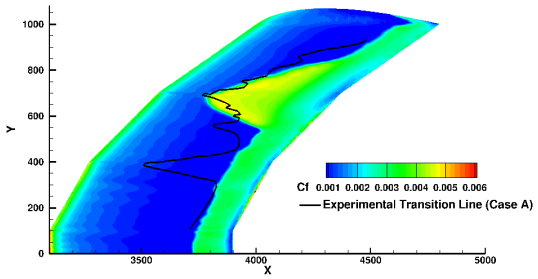

(a) Mesh 3 upper surface (20.3M cells)

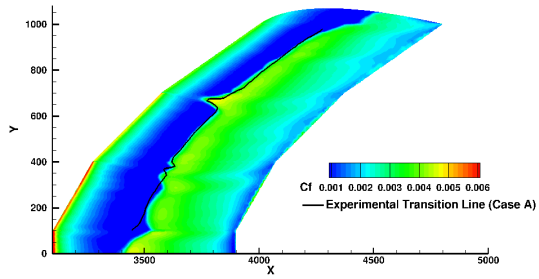

(b) Mesh 3 lower surface (20.3M cells)

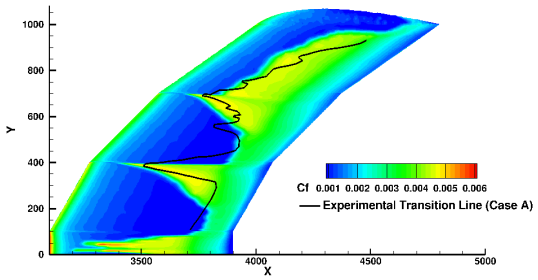

(c) Mesh 4 upper surface (20.7M cells)

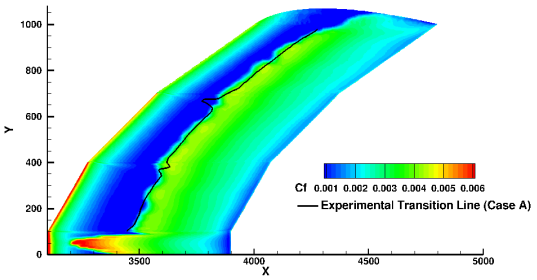

(d) Mesh 4 lower surface (20.7M cells)

Figure 4.22 Sickle Wing Case A Effect of mesh topology on skin friction using the $k\omega$-γ-$\tilde{R}e_{\theta t}$ model overlaid with experimental transition lines [1] ($Re = 2.75 \times 10^6, \alpha = -2.6°$)

CHAPTER 5 EFFECT OF SURFACE RUGOSITY ON AIRFOIL STALL

This chapter shows the results of the kω-γ-$\tilde{Re}_{\theta t}$ and SA-γ-$\tilde{Re}_{\theta t}$ models with the addition of the roughness Amplification model. Details of the equations and the implementation of the model can be found in Section 3.5. The goal is to model the effect of the surface roughness on the aircraft stall which is characterized by the loss of lift when the angle of attack increases too much.

5.1 Description of the Cases

The results of lift and drag curves are presented and compared to the experimental data from Abbott [34]. The drag curves are useful for validating the transition model since the drag will match the experimental data if the correct transition locations are replicated. The lift curves are useful to visualize the stall when the C_L starts decreasing. The results are produced using the following combination of flow conditions in order to examine the effect of each:

- Fully turbulent flow
- Transitional flow
- Transitional flow with roughness boundary condition
- Transitional flow with roughness and the Roughness amplification model

The selected cases for this study are the NACA23018 and NACA0009 airfoils. The NACA23018 is a thick airfoil with some camber compared to the NACA0009 which is a tinnier and symmetric airfoil. The flow conditions are a Mach number of 0.17, a Reynolds number of 6×10^6 and a freestream turbulence intensity of 0.05%. The simulations are performed on mesh of size 512×157 with Δs of 4.5×10^{-6} in order to have a $y+$ of less than 1. The meshes were generated using a custom mesh generation algorithm developed for 2D airfoils, detailed in Appendix B. In the experiment, 8% of the chord from the leading edge has the surface cover with 0.011 inches carborundum grains [34] for a chord length of 24 inches. Therefore, the equivalent sand roughness height (k_s), normalize by the chord, is 4.583×10^{-4}.

5.2 NACA23018 airfoil

Figure 5.1 and 5.2 respectively present the lift curve and drag curve of the NACA23018 for each model configuration and the effect of the roughness. The results are compared to the experimental data from Abbott [34].

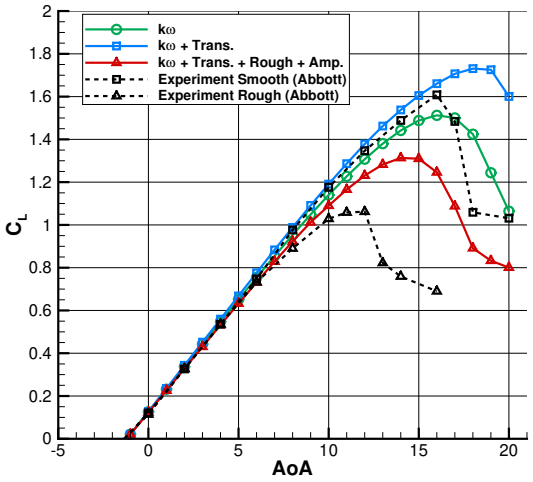

(a) $k\omega$-based turbulence models

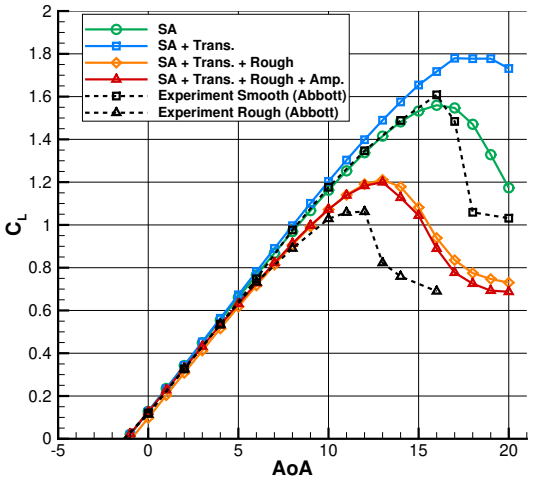

(b) SA-based turbulence models

Figure 5.1 Effect of the transition and roughness models on the lift curve of the NACA23018 airfoil ($M = 0.17, Re = 6 \times 10^6, Tu_\infty = 0.05\%, grid = 512 \times 157$)

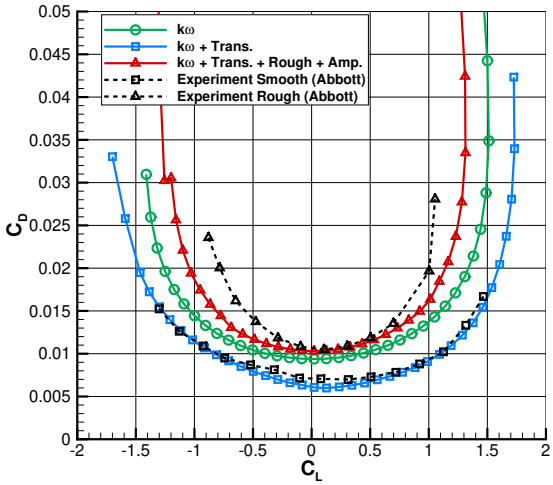

(a) $k\omega$-based turbulence models

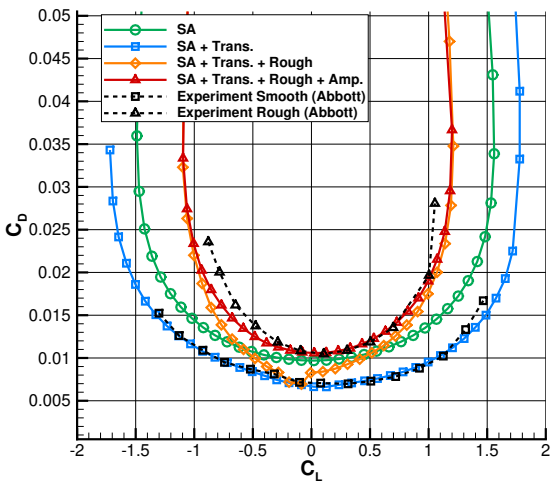

(b) SA-based turbulence models

Figure 5.2 Effect of the transition and roughness models on the drag curve of the NACA23018 airfoil ($M = 0.17, Re = 6 \times 10^6, Tu_\infty = 0.05\%, grid = 512 \times 157$)

5.2.1 Effect of the transition on stall

In Figure 5.1, the lift curves match very accurately with the experimental data in the linear region. As the angle of attack increases, the flow separation begins to negatively affect lift generation, causing the curve to become non-linear. For the fully turbulent simulations with the $k-\omega$ and SA models, the lift seems to be closer to the experimental data near the stall. However, this is a false positive since having fully turbulent flow is not representative of the reality since the transition is missing. Adding the transition to the $k\omega$-γ-$\tilde{R}e_{\theta t}$ and SA-γ-$\tilde{R}e_{\theta t}$ models cause an increase in the lift, maximum lift and maximum angle of attack in the non-linear region, overestimating the stall. This is caused by the transition delaying the start of the growth of the turbulent boundary layer thickness and as a result reduces the lift. This is expected as RANS models have usually inaccurate stall prediction in the literature [39, 40]. Moreover, the overshoot of the prediction of the stall for the $k\omega$-γ-$\tilde{R}e_{\theta t}$ model is somewhat smaller compared to the SA-γ-$\tilde{R}e_{\theta t}$ model.

5.2.2 Effect of the roughness on stall

The addition of the roughness amplification model causes a decrease of the lift, maximum lift and maximum angle of attack, as seen in Figure 5.1. The lift is overestimated compared to the experimental data in the non-linear region. However, the effect of roughness is well reproduced for the SA-γ-$\tilde{R}e_{\theta t}$ model since the offset with the experimental curve seems consistent with the offset without roughness. For the $k\omega$-γ-$\tilde{R}e_{\theta t}$ model, the roughness effect is not as strong and representative as the one with the SA-γ-$\tilde{R}e_{\theta t}$ model. But the two models do not have the same roughness boundary condition although they share the same transport equation for the roughness amplification model, which could explain the differences.

5.2.3 Effect of the transition on drag

The results of the corresponding drag curve are displayed on Figure 5.2. The drag of the fully turbulent simulations is overestimated for all lift coefficients despite them being inline with the experimental lift curves in Figure 5.3. On the contrary, the drag matches accurately with the experimental data when using transition models, which means that the transition locations are well predicted. This demonstrates the significant influence of the transition on the drag.

5.2.4 Effect of the roughness on drag

In Figure 5.2, the addition of the roughness amplification model causes an increase in the drag, as expected. For higher angles of attack, both negative and positive, the effect of the roughness of the drag is more accurate for the SA-γ-$\tilde{R}e_{\theta t}$ model then the $k\omega$-γ-$\tilde{R}e_{\theta t}$ model. Moreover, the effect of having the roughness amplification model compared to the simulation with the roughness boundary condition only is beneficial, as the effect of the roughness is local and global.

5.3 NACA0006 airfoil

The effect of roughness on the lift curves for the NACA0009 airfoil is displayed on Figure 5.3 for the $k\omega$-γ-$\tilde{R}e_{\theta t}$ and SA-γ-$\tilde{R}e_{\theta t}$ models. The lift matches the experimental data in the linear zone and is overestimated for higher angle of attack, which is consistent with the results of the NACA23018 airfoil in Section 5.2. However, the stall is sharper than experimental data which is the opposite of the NACA23018 airfoil. For the SA-γ-$\tilde{R}e_{\theta t}$ model, the effect of the roughness is well represented since the offset with the experimental data is similar to the offset without roughness.

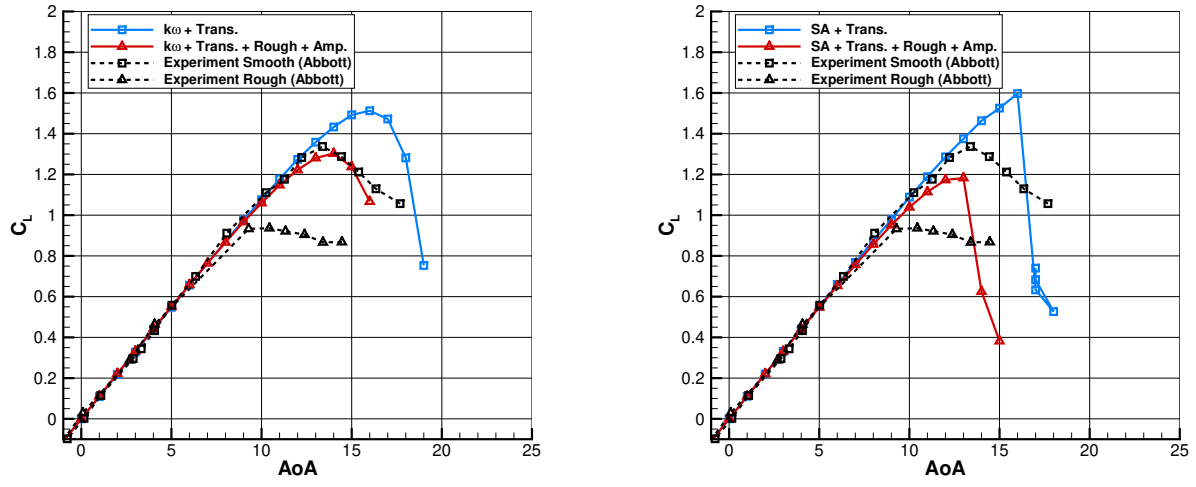

(a) $k\omega$-based turbulence models

(b) SA-based turbulence models

Figure 5.3 Effect of the transition and roughness models on the lift curve of the NACA0009 airfoil ($M = 0.17, Re = 6 \times 10^6, Tu_\infty = 0.05\%, grid = 512 \times 157$)

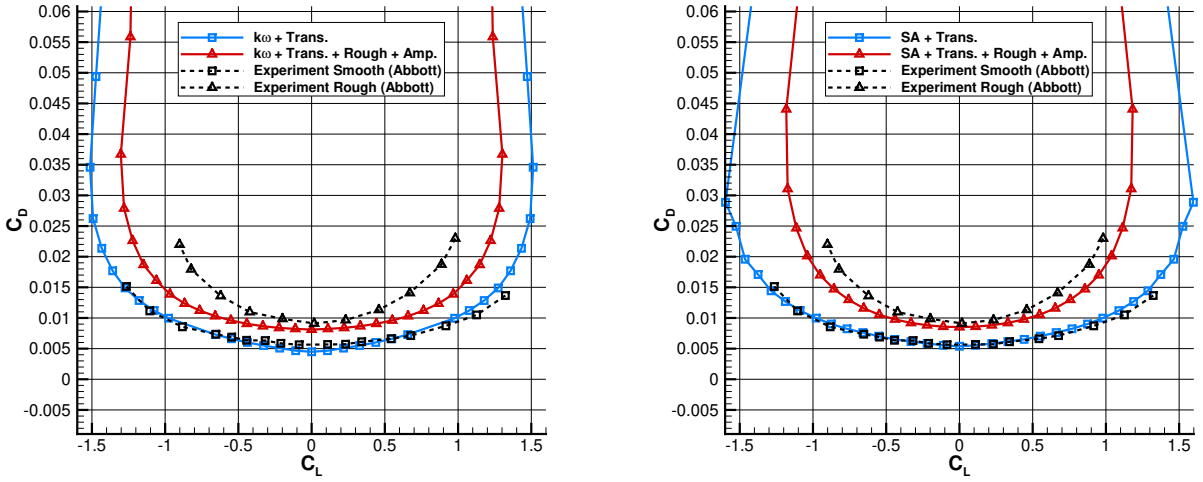

(a) $k\omega$-based turbulence models

(b) SA-based turbulence models

Figure 5.4 Effect of the transition and roughness models on the drag curve of the NACA0009 airfoil ($M = 0.17, Re = 6 \times 10^6, Tu_\infty = 0.05\%, grid = 512 \times 157$)

5.4 Model Improvement

The results have shown that the maximum lift is overestimated in both cases. Since it is a common issue with RANS models, Liang [40] proposed to calibrate two constants of the $k - \omega$ model to improve the stall characteristics: either decrease the a_1 constant or increase the $\beta*$ constant. The reader is referred to the original publication for an explanation. Figure 5.5 presents the results of simulations with small increases of $\beta*$. It shows that increasing $\beta*$ reduces the maximum lift coefficient without affecting the results in the linear region. The curve is more inline with the experimental data when using $\beta* = 0.10$. For the drag, the calibration did not also change the results inside the linear region, but it did increase drag for higher angles of attack.

For the SA turbulence model, Shelton and al. [39] conducted a study with the similar goal of improving the stall characteristics of the RANS models. It is proposed to reduce the parameter C_{v1} of the SA model which has an effect of changing the intercept of the viscous sublayer with the log law of the wall [39]. The default value of the constant is 7.1. Figure 5.6 compares the lift and drag curves using the parameter C_{v1} calibrated to 4.0 to the simulation with the default value. The stall prediction is indeed improved and the lift of the linear region is unchanged, as desired. However there is an overall increase of the drag which worsens the

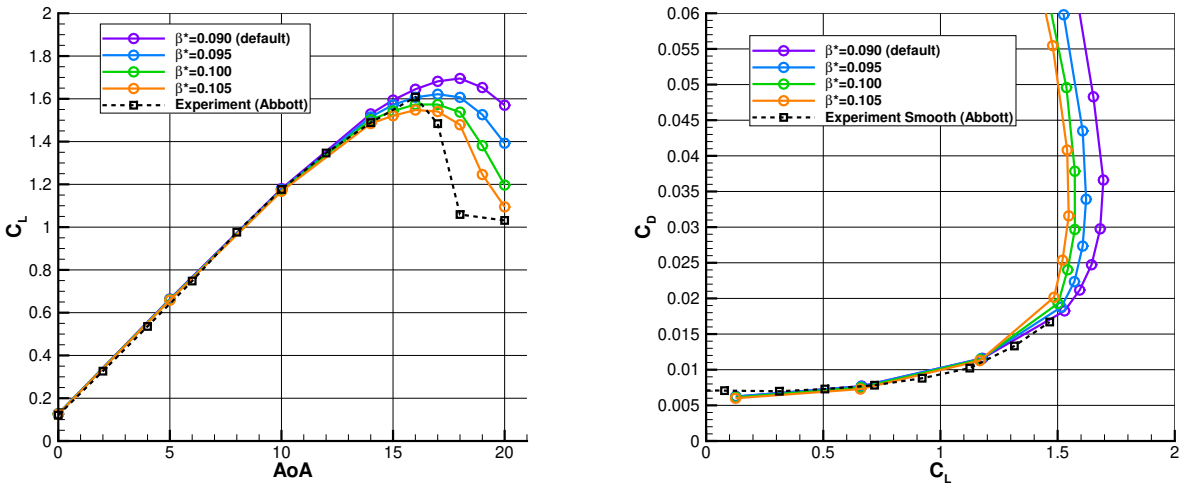

(a) Lift curve (b) Drag curve

Figure 5.5 Calibration of the $k-\omega$-based models using $\beta*$ to improve the stall prediction on the NACA23018 airfoil ($M = 0.17, Re = 6 \times 10^6, Tu_\infty = 0.05\%, grid = 512 \times 157$)

results in comparison to the experimental data.

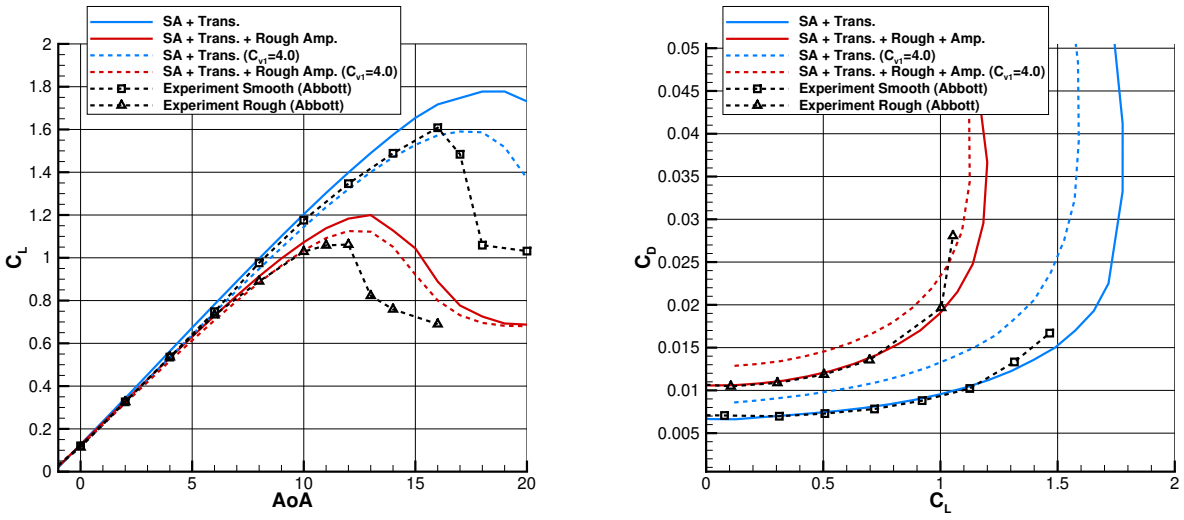

(a) Lift curve (b) Drag curve

Figure 5.6 Calibration of the SA-based models using C_{v1} to improve the stall prediction on the NACA23018 airfoil ($M = 0.17, Re = 6 \times 10^6, Tu_\infty = 0.05\%, grid = 512 \times 157$)

CHAPTER 6 CONCLUSION

6.1 Summary of Works

In conclusion, the presence of contaminants on aircraft wings increases roughness, which can alter the stall characteristics, the growth of turbulence and the drag. As physical testing of this effect is expensive and time-consuming, the main objective of this research project was to model this effect using turbulence, transition, and roughness models in a 3D CFD RANS solver. The understanding of how roughness impacts aircraft stall characteristics and turbulence growth with CFD methods can be used to design aircraft with better performance and safety.

The methodology used in this research project involved implementing the Spalart-Allmaras and $k-\omega$ SST turbulence models coupled to the γ-$\tilde{R}e_{\theta t}$ model transition model. The turbulence intensity was computed differently for each model, with the $k\omega$-γ-$\tilde{R}e_{\theta t}$ model using a locally computed value and the SA-γ-$\tilde{R}e_{\theta t}$ model using a constant value. The natural and by-pass transition correlations were solved using the Newton method, and the converged solution was reused to reduce computational cost. Smooth variants of the F_{length} and Re_{θ_c} correlations were implemented, but did not improve convergence. Calibration of the parameters c_{opt1} and c_{opt4} was also investigated, but the original values were ultimately retained. Relaxing the update of the conservative variable γ improved residual convergence and the maximum allowable time step.

Thereafter, the $k\omega$-γ-$\tilde{R}e_{\theta t}$ and SA-γ-$\tilde{R}e_{\theta t}$ transition model were compared. Both models were able to accurately predict separation-induced transition, but the $k\omega$-γ-$\tilde{R}e_{\theta t}$ model was better at predicting shear flow and separated flow. However, it could lead to the prediction of a separation bubble instead of natural transition, making the SA-γ-$\tilde{R}e_{\theta t}$ model more accurate for predicting natural transition even if the prediction was too early. In contrast, the $k\omega$-γ-$\tilde{R}e_{\theta t}$ model seems to be more accurate for predicting bypass transition as the length of the transition is somewhat too short for the SA-γ-$\tilde{R}e_{\theta t}$ model. In general, the two models seem to exhibit less accuracy with the natural transition. The natural transition is also being more sensitive to the grid resolution than the separation-induced transition. An investigation and correction were conducted for the SA-γ-$\tilde{R}e_{\theta t}$ model to improve early natural transition. The correction seemed to work as intended, and the already good results with separation-induced transition were unchanged.

The crossflow extension from Langtry was added to the models to include crossflow-induced transition for 3D cases. Both models were able to predict this type of transition when compared to experimental data on the prolate spheroid and sickle wing cases. The $k\omega$-γ-$\tilde{R}e_{\theta t}$ model was generally more accurate, but the SA-γ-$\tilde{R}e_{\theta t}$ model was less sensitive to mesh topology. However, the prediction of crossflow-induced transition for the SA-γ-$\tilde{R}e_{\theta t}$ model was too early. If calibrated, the SA-γ-$\tilde{R}e_{\theta t}$ model would be a more reliable and robust option for modelling crossflow-induced transition since the $k\omega$-γ-$\tilde{R}e_{\theta t}$ model experienced numerical difficulties and was more challenging to converge.

Finally, the surface roughness was modelled by adding a roughness amplification model. Different roughness boundary conditions from the literature were implemented for the $k-\omega$ and SA based models. The results were produced on two airfoil cases and the effect of the roughness was compared to the experimental data. Both models overestimate the stall characteristics, but the lift and the drag are accurately predicted in the linear region before the stall. The effect of roughness was more accurately reproduced with the SA-γ-$\tilde{R}e_{\theta t}$ model then with the $k\omega$-γ-$\tilde{R}e_{\theta t}$ model.

Overall, the objectives of this thesis have been successfully achieved by implementing turbulence, transition and roughness models in the CHAMPS software and validating them against experimental data. The results obtained showed good agreement with experimental results, though some aspects of the physics of the transition and aircraft stall were not fully captured. This work enables the use of CHAMPS for the design and analysis of aircraft with rough surfaces.

6.2 Recommendation

In most cases, the SA-γ-$\tilde{R}e_{\theta t}$ model is recommended over the $k\omega$-γ-$\tilde{R}e_{\theta t}$ model for simulating the transition and roughness effect. This recommendation is based on the following reasons:

- The SA-γ-$\tilde{R}e_{\theta t}$ model is numerically more stable, allowing for higher time steps and higher residual convergence rates.
- The SA-γ-$\tilde{R}e_{\theta t}$ model is easier to calibrate because the local turbulence intensity is constant and there is no decay of turbulence in the freestream.
- The accuracy of the SA-γ-$\tilde{R}e_{\theta t}$ model for transition is similar to the $k\omega$-γ-$\tilde{R}e_{\theta t}$ model

on average. However, the results of natural transition become more accurate when the correction developed in this work is applied. The SA-γ-$\tilde{R}e_{\theta t}$ model is also a promising option for modelling crossflow-induced transition if calibrated in future research.

- The SA-γ-$\tilde{R}e_{\theta t}$ model reproduces the roughness effect more accurately than the $k\omega$-γ-$\tilde{R}e_{\theta t}$ model, making it a robust option for modelling this effect.

6.3 Limitations

The following are the main limitations of the project:

- The transition models are based on empirical correlations which does not include the complete physic of the transition, and the accuracy of these correlations is uncertain as they are based on limited experimental data [16].
- The RANS model is limited to small-scale turbulence simulation using the eddy viscosity as it does not capture the large-scale turbulence like LES and DNS models would.
- The models are based on non-Galilean invariant parameters such as the freestream velocity. Therefore, this project is limited to non-moving walls only.
- The simulations were compared with limited experimental data whose accuracy is uncertain.
- The effect of the surrounding wall of the wind-tunnel experiments are very often neglected. Farfield boundary conditions are used instead of meshing the wind tunnel. The effect of these walls on the transition is uncertain, yet the comparative analysis of the sickle wing results suggested the meshing of the wind tunnel can have a significant impact on the crossflow-induced transition since the results were less accurate when using a farfield shaped domain.
- Depending on the case, the maximum allowable time step is limited by the stiffness and numerical instabilities of the models, which affects the residual convergence, especially with the $k\omega$-γ-$\tilde{R}e_{\theta t}$ model.

6.4 Future Research

- The accuracy of the correlations used in the models can be improved with more experiments on more variety of flow condition, as some of them were lacking the effect of the high-pressure gradient seen at high angles of attack, for example. The F_{length} correlation would also benefit from a better calibration, as some results had too short or too long transition region, especially with the SA-γ-$\tilde{R}e_{\theta t}$ model.
- The effect on the transition of the surrounding walls in the wind tunnel could be studied in order to know if the hypothesis that they can be neglected during simulations is valid.
- The correction for the early natural transition on the SA-γ-$\tilde{R}e_{\theta t}$ model could also be tested with the $k\omega$-γ-$\tilde{R}e_{\theta t}$ model.
- A calibration is needed for the crossflow extension when used with the SA-γ-$\tilde{R}e_{\theta t}$ model in order to lower the triggering of the crossflow and push the transition downstream.
- The crossflow extension from Müller and al. [41] could be implemented to test and validate a different model.
- A more extensive calibration of the models is needed to improve the accuracy and the effect of roughness at high angles of attack since all results were overshooting the maximum lift and angle of attack.
- The roughness effect on stall should be validated for 3D cases since only 2D cases were presented in this work.

REFERENCES

[1] M. Kruse *et al.*, *Transition Prediction Results for Sickle Wing and NLF(1)-0416 Test Cases*, 2018. [Online]. Available: https://arc.aiaa.org/doi/abs/10.2514/6.2018-0537

[2] M. Piotrowski and D. W. Zingg, "Smooth local correlation-based transition model for the spalart-allmaras turbulence model," *AIAA Journal*, vol. 59, no. 2, pp. 474, 492, 2021.

[3] D. M. Somers, "Design and experimental results for the s809 airfoil," in *National Renewable Energy Laboratory*, Golden, Colorado, 1989.

[4] ——, "Design and experimental results for a natural-laminar-flow airfoil for general aviation applications," in *NASA TP-1861*, NASA Langley Research Center Hampton, VA, 1981.

[5] G. B. Schubauer and P. S. Klebanoff, "Contributions on the mechanics of boundary-layer transition," 1956.

[6] N. Gregory and C. L. O'Reilly, "Low-speed aerodynamic characteristics of naca0012 airfoil section including the effects of upper surface roughness simulating hoar frost," in *TR, NPL AERO Rept. 1308,.* England, UK: Middlesex,, 1973.

[7] J. Anderson, *Fundamentals of aerodynamics*, 6th ed. Columbus, OH: McGraw-Hill Education, 2016.

[8] H. K. Versteeg and W. Malalasekera, *An Introduction to Computational Fluid Dynamics*, ser. International series of monographs on physics. Pearson Education Limited, 2007.

[9] R. B. Langtry, "A correlation-based transition model using local variables for unstructured parallelized cfd codes," in *Ph.D. thesis.* DLR, 2006.

[10] W. Slagter, "Cutting design costs: How industry leaders benefit from fast and reliable cfd," ANSYS INC., Tech. Rep., 2015. [Online]. Available: https://www.cadfem.net/fileadmin/user_upload/05-cadfem-informs/resource-library/wp-cfd-business-benefits.pdf

[11] S. Kurt and H. Yang, "Cfd simulation of aircraft icing effects using roughness modeling," in *62nd CASI Aeronautics Conference.* Bombardier, 2015. [Online].

Available: https://www.researchgate.net/publication/276248021_CFD_Simulation_of_Aircraft_Icing_Effects_using_Roughnes_Modeling

[12] P. Parenteau, S. Bourgault-Cote, and F. Plante, "Development of parallel cfd applications on distributed memory with chapel," *2020 IEEE International Parallel and Distributed Processing Symposium Workshops (IPDPSW)*, pp. 651, 658, 2020.

[13] P. R. Spalart and S. R. Allmaras, "A one equation turbulence model for aerodynamic flows," in *30th AIAA Aerospace Sciences Meeting and Exhibit.* Reno, Nevada: AIAA Paper 092-0439, 1992.

[14] F. R. Menter, "Two-equation eddy-viscosity turbulence models for engineering applications," *AIAA Journal*, vol. 32, no. 8, pp. 1598, 1605, 1994.

[15] J. H. Ferziger and M. Peric, *Computational Methods for Fluid Dynamics.* Springer, 2002.

[16] D. Pasquale, A. Rona, and S. J. Garret, "A selective review of cfd transition models," in *39th AIAA Fluid Dynamics Conference*, San Antonio, Texas, 2009.

[17] J. Smagorinsky, "General circulation experiments with the primitive equations," *Monthly Weather Review*, vol. 91, no. 3, pp. 99–164, 1963.

[18] M. Germano *et al.*, "A dynamic subgride-scale eddy viscosity model," *Journal Physic of Fluids*, vol. A 3, no. 7, pp. 1760–1765, 1991.

[19] B. Blocken, "Les over rans in building simulation for outdoor and indoor applications: A foregone conclusion?" *Building Simulation*, pp. 821–870, 2018.

[20] R. B. Langtry and F. R. Menter, "Correlation-based transition modeling for unstructured parallelized computational fluid dynamics codes," *AIAA Journal*, vol. 47, no. 12, pp. 2894, 2906, 2009.

[21] M. Piotrowski and D. W. Zingg, "Investigation of a correlation-based transition model in a newton-krylov algorithm," in *AIAA Scitech 2019 Forum.* San Diego, California: American Institute of Aeronautics and Astronautics, 2019.

[22] S. Medida and J. Baeder, "Application of the correlation-based gamma-re theta t transition model to the spalart-allmaras turbulence model," in *20th AIAA Computational Fluid Dynamics Conference.* Honolulu, HI: AIAA Paper 2011-3979, 2011.

[23] C. M. Langel *et al.*, *A Computational Approach to Simulating the Effects of Realistic Surface Roughness on Boundary Layer Transition*, 2014. [Online]. Available: https://arc.aiaa.org/doi/abs/10.2514/6.2014-0234

[24] A. Hellsten *et al.*, *Extension of the k-omega-SST turbulence model for flows over rough surfaces*, 2012. [Online]. Available: https://arc.aiaa.org/doi/abs/10.2514/6.1997-3577

[25] P. A. Durbin *et al.*, "Rough Wall Modification of Two-Layer k," *Journal of Fluids Engineering*, vol. 123, no. 1, pp. 16–21, 11 2000. [Online]. Available: https://doi.org/10.1115/1.1343086

[26] B. Aupoix and S. P. R, "Extensions of the spalart–allmaras turbulence model to account for wall roughness," *International Journal of Heat and Fluid Flow*, vol. 24, pp. 454–462, 2003.

[27] P. Dassler, D. Kozulovic, and A. Fiala, "Modelling of roughness-induced transition using local variables," pp. 14–17, 07 2010.

[28] C. Bilodeau-Bérubé, M. Blanchet, and E. Laurendeau, "Comparison of a correlation-based transitional model coupled to sa and kw-sst turbulence models," *AIAA AVIATION 2022 Forum*, 2022. [Online]. Available: https://arc.aiaa.org/doi/abs/10.2514/6.2022-3973

[29] NASA. (2021) Turbulence modeling resource. Langley Research Center. [Online]. Available: https://turbmodels.larc.nasa.gov/

[30] B. Barouillet, E. Laurendeau, and H. Yang, "On the calibration of the transitional k-w-gamma-rethetat turbulence model," in *AIAA Scitech 2021 Forum*. AIAA Paper 2021-0629, 2021.

[31] A. Mosahebi and E. Laurendeau, "Introduction of a modified segregated numerical approach for efficient simulation of -r~et transition model," *International Journal of Computational Fluid Dynamics*, vol. 29, no. 6-8, pp. 357, 375, 2015.

[32] R. B. Langtry *et al.*, "Extending the gamma-rethetat correlation based transition model for crossflow effects," in *45th AIAA Fluid Dynamics Conference*. AIAA Paper 2015-2474, 2015.

[33] B. Aupoix, "Wall roughness modelling with k-w stt model," 09 2014.

[34] I. H. Abbott and A. E. Von Doenhoff, *Theory of Wing Sections: Including a Summary of Airfoil Data*. Mineola: Dover Publications, 1959.

[35] J. G. Coder, "Standard test cases for transition model verification and validation in computational fluid dynamics," in *2018 AIAA Aerospace Sciences Meeting*. AIAA Paper 2018-0029, 2018.

[36] S. Nie, "Extension of transition modeling by a transport equation approach," 2017.

[37] A. M. Savill, "Some recent progress in the turbulence modeling of by-pass transition," in *Near-wall turbulent flows*, 1993, pp. 829–848.

[38] R. Petzold and R. Radespiel, *Transition on a Wing with Spanwise Varying Crossflow Evaluated with Linear Stability Theory*, 2015. [Online]. Available: https://arc.aiaa.org/doi/abs/10.2514/6.2013-2466

[39] A. Shelton *et al.*, *Improving the CFD Predictions of Airfoils in Stall*, 2005. [Online]. Available: https://arc.aiaa.org/doi/abs/10.2514/6.2005-1227

[40] C. Liang, "Effect of closure coefficients of k-w sst turbulence model on predicting stall characteristics of the airfoil," *Journal of Physics: Conference Series*, vol. 1600, no. 1, p. 012032, jul 2020. [Online]. Available: https://doi.org/10.1088/1742-6596/1600/1/012032

[41] C. Müller-Schindewolffs and F. Herbst, "Modelling of crossflow-induced transition based on local variables," 07 2014.

APPENDIX A FINITE VOLUME METHOD

The equations of the models are discretized using the finite volume method. This appendix describes the main steps to transform the equations into their solvable form. The k-ω-SST model is used as an example, but the same methodology applies to other model equations. The first step is to integrate the two transport equations over a finite volume of a cell Ω:

$$\int_\Omega \frac{\partial(\rho k)}{\partial t} d\Omega + \int_\Omega \frac{\partial(\rho u_j k)}{\partial x_j} d\Omega - \int_\Omega \frac{\partial}{\partial x_j}\left[(\mu + \sigma_k \mu_t)\frac{\partial k}{\partial x_j}\right] d\Omega = \int_\Omega P - \beta^* \rho \omega k d\Omega \tag{A.1}$$

$$\int_\Omega \frac{\partial(\rho \omega)}{\partial t} d\Omega + \int_\Omega \frac{\partial(\rho u_j \omega)}{\partial x_j} d\Omega - \int_\Omega \frac{\partial}{\partial x_j}\left[(\mu + \sigma_\omega \mu_t)\frac{\partial \omega}{\partial x_j}\right] d\Omega = \int_\Omega \frac{\gamma}{\nu_t} P - \beta \rho \omega^2 + 2(1-F_1)\frac{\rho \sigma_{\omega 2}}{\omega}\frac{\partial k}{\partial x_j}\frac{\partial \omega}{\partial x_j} d\Omega \tag{A.2}$$

The variables of the first term of the equations are independent from the volume and the integral can be directly solved. The second and third terms are respectively the integral of the convective and diffusive fluxes over a volume. Therefore, the divergence theorem is used to transform them into an integral of the flux through the close surface (S) of the cell. The right-hand side of the equations are the source terms and their variables are also independent of the volume and the integral can be solved directly. The new equations are the following:

$$\frac{\partial(\rho k)}{\partial t}\Omega + \oint_S \rho k \vec{u} \cdot \vec{n} dS - \oint_S \left[(\mu + \sigma_k \mu_t)\frac{\partial k}{\partial x_j}\right] \cdot \vec{n} dS = (P - \beta^* \rho \omega k)\Omega \tag{A.3}$$

$$\frac{\partial(\rho \omega)}{\partial t}\Omega + \oint_S \rho \omega \vec{u} \cdot \vec{n} dS - \oint_S \left[(\mu + \sigma_\omega \mu_t)\frac{\partial \omega}{\partial x_j}\right] \cdot \vec{n} dS = (\frac{\gamma}{\nu_t} P - \beta \rho \omega^2 + 2(1-F_1)\frac{\rho \sigma_{\omega 2}}{\omega}\frac{\partial k}{\partial x_j}\frac{\partial \omega}{\partial x_j})\Omega \tag{A.4}$$

Since the equations are being solved for each cell of a mesh and the geometry of each cell is known, the flux can be calculated on the faces of each cell. Therefore, the surface integrals can be rewritten as a sum over each face of the cell. The scalar product of the velocity with the normal of each face is renamed as the contravariant velocity (V):

$$V = n_x u + n_y v + n_z w \tag{A.5}$$

The convective flux vector is then defined as:

$$\vec{F_c} = \begin{bmatrix} \rho k V \\ \rho \omega V \end{bmatrix} \tag{A.6}$$

and the viscous flux vector is defined as:

$$\vec{F_v} = \begin{bmatrix} n_x \tau_{xx}^k + n_y \tau_{yy}^k + n_z \tau_{zz}^k \\ n_x \tau_{xx}^\omega + n_y \tau_{yy}^\omega + n_z \tau_{zz}^\omega \end{bmatrix} \tag{A.7}$$

with:

$$\tau_{xx}^k = (\mu + \sigma_k \mu_t)\frac{\partial k}{\partial x}, \tau_{yy}^k = (\mu + \sigma_k \mu_t)\frac{\partial k}{\partial y}, \tau_{zz}^k = (\mu + \sigma_k \mu_t)\frac{\partial k}{\partial z} \tag{A.8}$$

$$\tau_{xx}^\omega = (\mu + \sigma_\omega \mu_t)\frac{\partial \omega}{\partial x}, \tau_{yy}^\omega = (\mu + \sigma_\omega \mu_t)\frac{\partial \omega}{\partial y}, \tau_{zz}^\omega = (\mu + \sigma_\omega \mu_t)\frac{\partial \omega}{\partial z} \tag{A.9}$$

The source term vector is defined as:

$$\vec{Q} = \begin{bmatrix} P - \beta^* \rho \omega k \\ \frac{\gamma}{\nu_t} P - \beta \rho \omega^2 + 2(1 - F_1)\frac{\rho \sigma_{\omega 2}}{\omega}\frac{\partial k}{\partial x_j}\frac{\partial \omega}{\partial x_j} \end{bmatrix} \tag{A.10}$$

The conservative variable vector is defined as:

$$\vec{W} = \begin{bmatrix} \rho k \\ \rho \omega \end{bmatrix} \tag{A.11}$$

Finally, the conservative variables are discretized over time steps Δt. The system of equations can be written as the following:

$$\frac{\Delta \vec{W}}{\Delta t}\Omega + \sum_j^{nface} (\vec{F_c} - \vec{F_v}) S_j = \vec{Q}\Omega \tag{A.12}$$

The system of equations is used in a pseudo-time accurate scheme and solved using an explicit Runge-Kutta or an implicit backward-Euler algorithm in which the linear systems are solved with a Block SGS scheme or a GMRES solver [12]. For simplicity, only the explicit scheme is detailed in the following. The residual vector is defined:

$$\vec{R^i} = \frac{\Delta \vec{W}}{\Delta t}\Omega = \vec{Q}\Omega - \sum_j^{nface} (\vec{F_c} - \vec{F_v}) S_j \tag{A.13}$$

$$\Delta \vec{W}^i = \frac{\Delta t}{\Omega} \vec{R}^i \tag{A.14}$$

APPENDIX B MESH GENERATION ALGORITHM FOR AIRFOILS

A simple mesh generation algorithm was developed to quickly generate a O-type grid for any airfoils geometry with thin trailing edge.

Inputs

- the number of points of the airfoil geometry: N_a
- the coordinates of each point of the airfoil geometry
- the desired number of steps in the normal direction (j): N_s
- the initial step size in the normal direction: Δs_0
- the growth rate between each step: r

Function 1

Each step size (Δs_j), is computed with the following:

$$\Delta s_j = \Delta s_0 \cdot r^j, \quad j = \{0, N_s - 1\} \tag{B.1}$$

Function 2

For each i node in a *for loop*, the neighbouring faces normal ($\vec{n}_{face}$) and the face lengths (Δ_l) are computed. Then, the nodes normal ($\vec{n}_{node}$) are computed with the following algorithm:

$$\vec{n}_{node,i,j} = \begin{bmatrix} n^L_{face,x} F^L + n^R_{face,x} F^R \\ n^L_{face,y} F^L + n^R_{face,y} F^R \end{bmatrix} \tag{B.2}$$

$$\vec{n}_{face} = \begin{bmatrix} n_{face,x} \\ n_{face,y} \end{bmatrix} \tag{B.3}$$

$$F^L = \frac{\Delta l^L}{\Delta l^L + \Delta l^R} \tag{B.4}$$

$$F^R = \frac{\Delta l^R}{\Delta l^L + \Delta l^R} \tag{B.5}$$

with L and R designating the left and right faces of the i node.

Function 3 (main)

For each j step in a *for loop*:

1. Compute Δs_j with function 1
2. Compute $\vec{n}_{node,i,j}$ with function 2 using the $\vec{n}_{face,i,j}$. However, it is recommended to only used the $\vec{n}_{face,i,j}$ for $j = 0$ as explained in function 2, then used the $\vec{n}_{node,i,j-1}$ of the previous iteration to compute the $\vec{n}_{node,i,j}$. It is also recommended to perform sub-iteration between $j-1$ and j to compute the final nodes normal to increase how fast the normals change direction which is useful for handling concave curves. Using relaxation (α) between sub-iteration is also recommended to prevent oscillations.
3. For each i node in a *for loop*, compute the next nodes coordinates:

$$\begin{bmatrix} x_{i,j+1} \\ y_{i,j+1} \end{bmatrix} = \begin{bmatrix} x_{i,j} \\ y_{i,j} \end{bmatrix} + \Delta s_j \cdot \vec{n}_{node,i,j} \tag{B.6}$$

Figure B.1 shows an example of mesh generated using the NACA95110 airfoil, selected for its strong convex and concave curves. Note that it is left to the user to decide how to write the connectivity between the nodes and elements and pass this information to the solver.

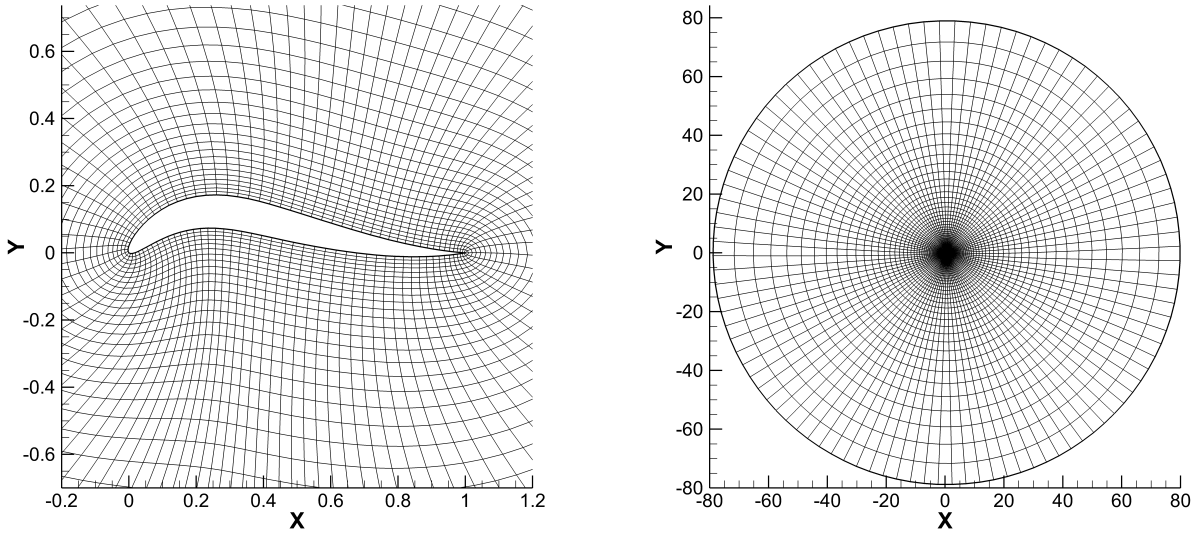

(a) Close view (b) Far view

Figure B.1 Mesh generated from a NACA95110 airfoil geometry using $N_a = 100$, $N_s = 70$, $\Delta s_0 = 0.01$, $r = 1.10$, 8 sub-iterations and $\alpha = 0.9$ for diverging normals only

APPENDIX C OTHER RESULTS OF THE SICKLE WING CASE

This appendix presents additional results for cases B and C of the sickle wing, which were introduced in Section 4.3.2. These results were obtained using Mesh 1, which is a medium mesh with 8.1 cells, as detailed in Table 4.3.

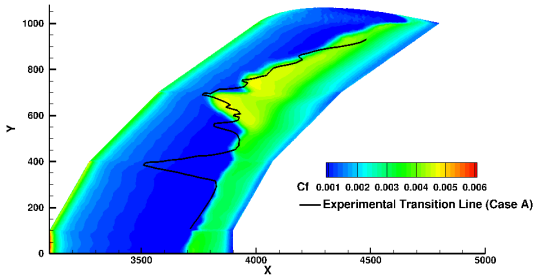

(a) $k\omega$-γ-$\tilde{R}e_{\theta t}$ model (upper surface)

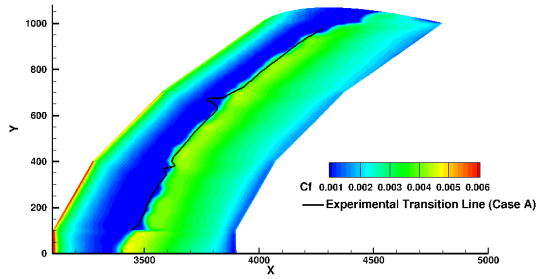

(b) $k\omega$-γ-$\tilde{R}e_{\theta t}$ model (lower surface)

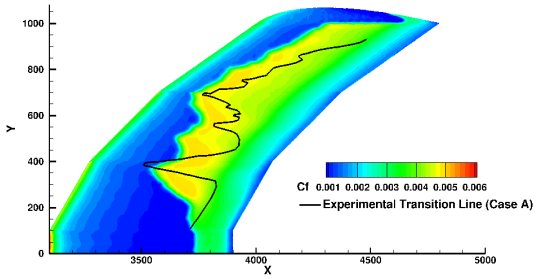

(c) SA-γ-$\tilde{R}e_{\theta t}$ model (upper surface)

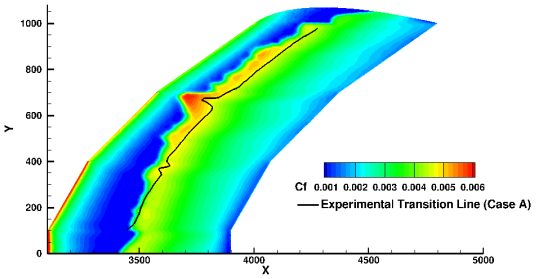

(d) SA-γ-$\tilde{R}e_{\theta t}$ model (lower surface)

Figure C.1 Sickle Wing Case A skin friction using Mesh 1 overlaid with experimental transition lines from Kruze & al. [1] ($Re = 2.75 \times 10^6, \alpha = -2.6°$)

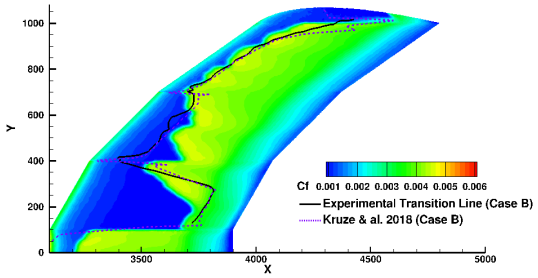

(a) $k\omega$-γ-$\tilde{Re}_{\theta t}$ model (upper surface)

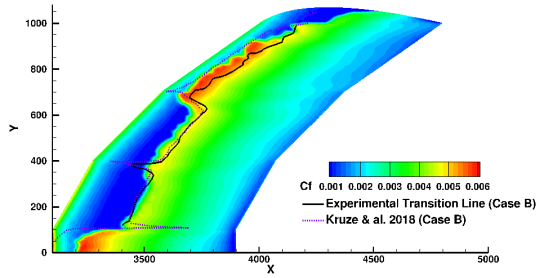

(b) $k\omega$-γ-$\tilde{Re}_{\theta t}$ model (lower surface)

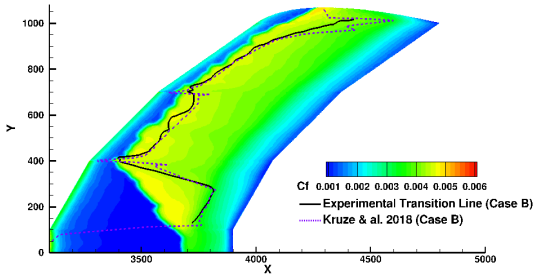

(c) SA-γ-$\tilde{Re}_{\theta t}$ model (upper surface)

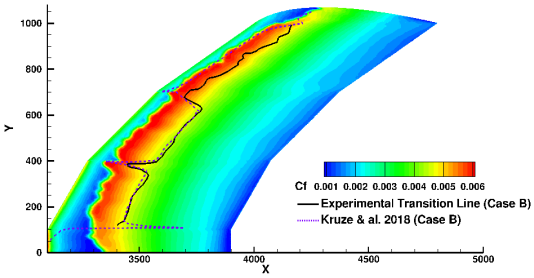

(d) SA-γ-$\tilde{Re}_{\theta t}$ model (lower surface)

Figure C.2 Sickle Wing Case B skin friction using Mesh 1 overlaid with experimental and predicted transition lines from Kruze & al. [1] ($Re = 4.50 \times 10^6, \alpha = -2.6°$)

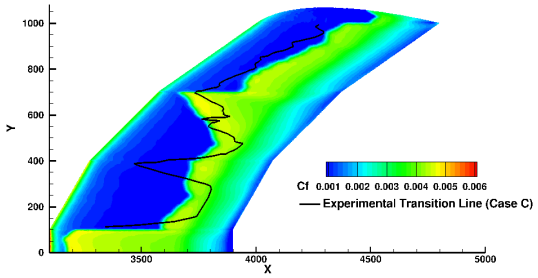

(a) $k\omega$-γ-$\tilde{Re}_{\theta t}$ model (upper surface)

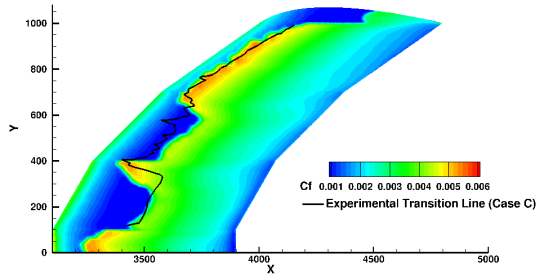

(b) $k\omega$-γ-$\tilde{Re}_{\theta t}$ model (lower surface)

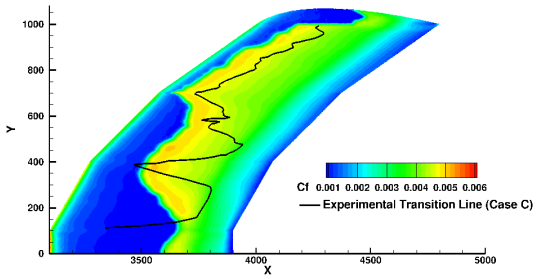

(c) SA-γ-$\tilde{Re}_{\theta t}$ model (upper surface)

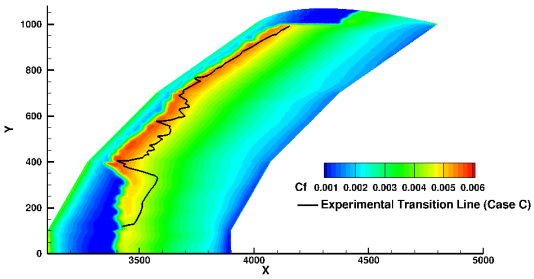

(d) SA-γ-$\tilde{Re}_{\theta t}$ model (lower surface)

Figure C.3 Sickle Wing Case C skin friction using Mesh 1 overlaid with experimental transition lines from Kruze & al. [1] ($Re = 4.50 \times 10^6, \alpha = -2.6°$)